Data Analysis of Organics and Other Sources (Volatile Chemical Products) in the California South Coast Air Basin

Report to the

California Air Resources Board

Contract Number 22RD015

Prepared by:

John H. Seinfeld

California Institute of Technology

28 May 2025

Prepared for the California Air Resources Board and the California Environmental Protection Agency

The statements and conclusions in this Report are those of the contractor and not necessarily those of the California Air Resources Board. The mention of commercial products, their source, or their use in connection with material reported herein is not to be construed as actual or implied endorsement of such products.

Acknowledgment

The work described here was performed at the California Institute of Technology and was supported by Prof. Paul Wennberg, Dr. Reina Buenconsejo, Ms. Haroula Baliaka, Dr. Ben Schulze, Dr. Ryan Ward, and Dr. John Crounse. The authors would like to thank Dr. Nathan Dalleska for useful conversations regarding instrumentation.

This report was submitted in fulfillment of CARB contract number 22RD015, "Data Analysis of Organics and Other Sources (Volatile Chemical Products) in the California South Coast Air Basin" by the California Institute of Technology under the sponsorship of the California Air Resources Board. Work was completed as of December 31, 2024.

Table of Contents

List of Figures

List of Tables

Abstract

Atmospheric volatile organic compounds (VOCs) in the presence of NO_x chemically react to form photochemical smog. The VOCs in urban air typically derive from energy and transportation technologies, as well as the use of petro-chemical-derived products. A notable change is underway in United States cities, shifting from an urban atmosphere dominated by transportation-related VOCs to ones dominated by VOCs from volatile chemical products (VCPs): coatings, adhesives, and consumer products. At the same time, NO levels are decreasing across the US and in the Los Angeles Basin. Chemicals produced in the oxidation of VCPs are analyzed in a laboratory setting, using an environmental smog chamber. These tools enable study of how the secondary organic aerosol (SOA) yield changes with the abundance of NO. This project quantifies the secondary organic aerosol (SOA) yield of several important glycol ethers found in VCPs. The analysis reveals the importance of studying VCPs in the laboratory as a function of NO level to evaluate the SOA formation under environmental conditions that exist across California today.

In a second thrust, this project investigated the dynamics of ammonium nitrate (AN) aerosol. AN is often the primary inorganic component of urban smog and notoriously difficult to measure due to its volatility. Despite decades of progress in reducing nitrogen oxide (NO_x) emissions, AN levels remain elevated in Los Angeles (LA). Aerosol mass spectrometry data obtained over multiple years illustrates the controlling dynamics of AN and its evolution over the past decades. These data suggest that much of the nitric acid (HNO_3) production required to produce AN in LA occurs during the nighttime via heterogeneous hydrolysis of dinitrogen pentoxide (N_2O_5). Further, this research shows that while EPA-codified techniques for measuring total Particulate Matter (PM) often underestimate the AN component and thereby have a low bias in total aerosol mass, some low-cost optical sensors more accurately capture the total aerosol mass. While previous studies suggest declining NO_x has reduced AN, we show that HNO_3 formation is still significant and leads to the formation of many 10s of $\mu g\ m^{-3}$ of AN aerosol.

Executive Summary

Background

Air quality in California's South Coast Air Basin (SoCAB) has improved considerably over the past several decades because of regulatory policies aimed at curbing industrial and motor vehicle emissions. However, the past 10 – 15 years improvements in both total particulate matter (PM) and organic aerosol concentrations as reported by South Coast Air Quality Management District (AQMD) have slowed. The lack of continual improvement may be driven in part by the oxidation of volatile chemical products (VCPs) together with higher hydroxyl radical (OH) concentrations that result from reduced NO_x levels. Changes in the formation rate of ammonium nitrate (AN) are also important for understanding the PM trends. Laboratory experiments analyzing the chemistry of VCP components can help elucidate the role of VCPs in influencing current air quality trends. Study of the changes in AN formation can provide guidance on future changes in inorganic aerosol formation.

Objectives and Methods

The objective of this study was twofold. Part A evaluates the secondary organic aerosol (SOA) formation of VCP components in the Caltech environmental chamber as a function of NO_x levels. Glycol ethers germane to VCPs were studied to characterize the SOA formation in their oxidation chemistry and how the SOA yield is influenced by NO. Part B evaluates the changes in AN levels in SoCAB to understand how reductions in NO_x emissions have altered the formation of nitric acid (HNO_3) and thereby altered the chemistry controlling AN formation. In addition, this research used newly available instrumentation to evaluate the fidelity of AN quantification using standard Federal Methods.

Results

Part A. We analyzed two glycol ethers in the Caltech environmental chambers to quantify their SOA yields and assess their potential impact on aerosol formation in various settings. SOA yield experiments were conducted over a range of peroxy radical bimolecular lifetimes. These ethers offer a good model system for understanding how the large reductions on NO concentrations observed in the SoCAB may alter the formation yields of SOA. Thus, the laboratory investigation included conditions aimed to represent the range of environmental conditions experienced in different locations across California — from NO saturated regimes to areas where autoxidation may occur. SOA yields of ethoxyethanol range from 4.5 – 22% and correlate well with peroxy radical bimolecular lifetime; as the bimolecular lifetime increases, SOA yield increases. In the butoxyethanol system, the correlation is less clear. SOA yields of butoxyethanol range from 1 – 6%.

Part B. Aerosol mass spectrometry data obtained over multiple years in SoCAB illustrates the controlling dynamics of AN and its evolution over the past decades. These data suggest that much of the HNO_3 production required to produce AN in SoCAB occurs during the nighttime via heterogeneous hydrolysis of N_2O_5. Further, this analysis shows that EPA-codified techniques for measuring total $PM_{2.5}$ generally fails to accurately quantify the AN component, while some low-cost optical sensors demonstrate better quantification. This work also highlights the value of real-time speciated PM measurements for diagnosing the sources that contribute to aerosol pollution.

Conclusion

Part A. Analysis of glycol ethers in the Caltech environmental chambers provides insight into our understanding of the importance of VCPs. At sufficiently long bimolecular lifetimes, the ethoxyethanol peroxy radical will undergo H-shift autoxidation. For example, when the peroxy radical bimolecular lifetime is greater than 10 s (equivalent to [NO] of about 500 ppt), the intramolecular hydrogen shift accounts for approximately 30% of the reactive pathway. The lower SOA yields in the butoxyethanol system may reflect a decomposition reactions that occurs. While the analysis of the environmental chambers highlights some challenges with determining SOA formation potentials across a large class of compounds, based on computational chemical methods such as those previously reported by Yu et al., 2023, our study highlight the value of such computational methods for evaluating autoxidation rate coefficients across the wide diversity of organic chemicals present in the urban atmosphere.

Part B. Despite decades of progress in reducing NO_x emissions, AN remains the primary inorganic component of particulate matter (PM) in SoCAB. While previous studies suggest declining NO_x has reduced AN, we show that HNO_3 formation is still significant and leads to the formation of many 10s of μg m^{-3} of AN aerosol. Continued focus on reductions in NO_x will help meet the $PM_{2.5}$ standards in the LA basin and many other regions. Further efforts to evaluate the accuracy of quantification of AN using both EPA-codified techniques and low-cost sensors is warranted.

Part A: **The Formation of Secondary Organic Aerosol in the Oxidation of Glycol Ethers**

California Air Resources Board Contract Number 22RD015

A1. Introduction

Exposure to ambient aerosol is linked to an increased risk cardiovascular and respiratory disease, causing millions of premature deaths annually (Cohen et al., 2017; Burnett et al., 2019; Pye et al., 2021). In the U.S., mobile emission sources (i.e., on-road and non-road vehicles and equipment) have historically produced a considerable fraction of organic aerosol (OA) in urban areas (Watson et al., 1994; Schauer et al., 1996; Stone et al., 2009; Hasheminassab et al., 2014; McDonald et al. 2015; Ortega et al., 2016; Gentner et al., 2017). Vehicle operation produces OA through both direct particulate emissions, termed primary OA (POA), and via exhaust and/or evaporative emissions of gas-phase fuel components, which are oxidized to form secondary OA (SOA) (Gentner et al., 2017). Fuel combustion also leads to considerable nitrogen oxide (NO_x) emissions.

The Los Angeles Basin has historically experienced some of the highest aerosol concentrations in the country (Ensberg et al., 2013; Lawson et al., 1990; Docherty et al., 2011; Hayes et al., 2013) and has failed to attain compliance with the 2012 National Ambient Air Quality Standard for fine particulate matter ($PM_{2.5}$) concentrations (EPA, 2012). While implementation of regulatory policies such as the California Low-Emission Vehicle (LEV) program have successfully reduced gaseous and aerosol pollutant concentrations over the last seventy years (McDonald et al., 2015; Warneke et al., 2012; Pollack et al., 2013), aerosol concentrations measured in Los Angeles have remained relatively constant during the last decade, despite considerable declines in mobile source emissions of OA precursors (CEPAM, 2019).

Several factors may contribute to the recent trend in aerosol concentrations. Reductions in on-road aerosol precursor emissions (Hasheminassab et al., 2014; Altuwayjiri et al., 2021) have likely increased the relative importance of non-vehicular aerosol precursor sources such as volatile chemical products (VCPs) (Khare et al., 2018; McDonald et al., 2018; Khare et al., 2020; Seltzer et al., 2021a,b). VCPs include non-mobile emissions of solvents, pesticides, and personal care products which easily volatilize under typical atmospheric conditions vis a vis volatile organic compounds (VOCs). McDonald et al. (2018) suggested that in Los Angeles VCP emissions may be twice as large as VOC emissions from mobile sources and their oxidation likely contributes to a large fraction of SOA formation (Khare and Getner, 2018; McDonald et al., 2018; Pennington et al. 2021; Seltzer et al., 2021).

Previous CARB-funded research in collaboration with the University of California at Riverside (UCR) used VCPs precursors to understand the sensitivity of vapor wall loss to distribution of vapors and to compare chamber parameters between UCR and Caltech (CARB 18RD009). These studies characterized the SOA formation of cyclic compounds in a variety of different environments. For example, the SOA formation of benzyl alcohol was characterized as a function of temperature and NO_x (Charan et al., 2020). The SOA formation from Decamethylcyclopentasiloxane (D5 siloxane) oxidation was characterized as a function of OH exposure, elucidating the importance of selecting atmospherically-relevant OH exposures in laboratory experiments (Charan et al., 2022). The present experiments focused on the characterization of glycol ethers over a range of biomolecular lifetimes. The research presented in this report is particularly germane as glycol ethers were previously thought to have low SOA formation potential based on past research which studied these VCP precursors in primarily high NO conditions. However, this work indicates that glycol ethers may have a larger SOA formation potential in lower NO conditions where bimolecular lifetimes are large enough for autooxidation to occur.

Reductions in NO_x emissions may also increase PM formation efficiency of organic precursors through changes in atmospheric oxidation chemistry. Decreases in urban NO_x emissions have increased local hydroxyl radical (OH) concentrations by as much as 50% over the past few decades (Van Rooy., 2021), accelerated VOC oxidation and thereby increased the fraction of SOA precursors oxidized in the basin (Warneke et al., 2013; Kim et al., 2016; Van Rooy et al., 2021). Lower NO_x emissions could have also altered photochemical oxidation pathways and, in turn, increased SOA yields (defined as the amount of OA formed per mass of precursor oxidized) (Ng et al., 2007; Chan et al., 2009; Praske et al., 2018).

In this analysis, we aim to elucidate the role of several VCPs in driving current air quality trends. In the laboratory, two glycol ethers, ethoxyethanol (2-EE) and butoxyethanol (2-BE) were studied. Glycol ethers were selected for study because of their ubiquity in many VCPs, particularly cleaning products, cosmetics, and soaps (Singer et al., 2006; EPA, 2016). Acute and chronic exposure to glycol ethers can lead to human health effects such as narcosis, liver and kidney damage, and anemia (EPA, 2016). Emissions of glycol ethers are also significant to the outdoor atmosphere, with one study estimating more than 13 tons of glycol ether emitted per day in the state of California (Cocker et al., 2014). 2-EE and 2-BE are both considered members of the E-series glycol ethers and are included in the Prop 65 list, and may being phased out or replaced due to toxicity concerns. 2-EE and 2-BE are considered IVOCs. Other short-chain glycol ethers such as ethylene glycol dimethyl ether are considered VOCs. Though 2-EE is also a short-chain compound, the terminal hydroxyl (-OH) group lowers its volatility due to the strong C-O intermolecular bonding.

A2. Materials and Methods

A.2.1 Laboratory description

SOA yields were evaluated in the Caltech environmental chamber which consists of two ~19 m^3 FEP (fluorinated ethylene propylene) Teflon reactors. One reactor was used exclusively for low NO_x experiments and one reactor was used for high NO_x experiments. The Caltech environmental chambers were temperature (20 – 45°C) and humidity (0 – 100%) controlled. Prior to each experiment, the reactors were flushed continuously with purified air for > 24 h at ~30 psi.

Irradiation in the chamber was initiated using fluorescent black mercury lamps which are housed on either side of the chamber. All other surfaces of the chamber were covered in reflective metal sheeting. The mercury lamps have a maximum wavelength peak at 355 nm and $k_{NO2->NO}$ of 0.372 min^{-1}. The intensity of the lights was adjustable (0 – 100%).

Injections into and sampling out of the reactors were done with the minimal amount of sample tubing possible to minimize tubing wall loss. VOC and oxidant injections and sampling were done using Teflon tubing, while aerosol injection and sampling were done using stainless steel tubing. Hydrogen peroxide (H_2O_2) was the oxidant source and was injected by blowing purified air over aliquots of H_2O_2 warmed in a ~42°C water bath. Seed aerosol was injected into the chamber by bubbling purified air through an aqueous (MilliQ) solution of ammonium sulfate ($(NH_4)_2SO_4$) (0.06 M). Particles were dried using a black carbon denuder and charge neutralized using a soft X-ray neutralizer. NO (506.2 ppm ± 2%, Airgas) injections directly from the gas cylinder were timed to achieve the desired mixing ratio. Adequate NO was injected such that there was always NO remaining at the end of the experiment. In some experiments, methanol (CH_3OH, Sigma-Aldrich, >99.9%) was injected to adjust the HO_2 mixing ratio. Methanol forms HO_2 by reacting with OH in the presence of molecular oxygen to form HO_2, HCHO, and H_2O. Though OH formed from the photolysis of H_2O_2 also forms HO_2 ($OH + H_2O_2 -> HO_2 + H_2O$), the mixing ratio of HO_2 is dominated by the methanol pathway. IVOC precursors were injected by placing a known volume and mass of the IVOC on a Teflon filter and blowing warmed, filtered air over. Ethylene glycol (Sima-Aldrich, 99.8%) was used as a tracer and was injected in a similar manner as the IVOC precursors.

Table A1: Summary of experimental conditions for oxidation of 2-EE and 2-BE**.** Methanol is used to vary the amount of HO_2 in the system. All experiments were performed at 23 ºC with the exception of BE2.

Expt No.	VOC	MeOH (ppm)	NO (ppb)	Lights (%)	Temp
EE1	Ethoxyethanol	0	0	100	23
EE2	Ethoxyethanol	45	0	100	37
EE3	Ethoxyethanol	45	0	33	23
EE4	Ethoxyethanol	45	0	100	23
EE5	Ethoxyethanol	0	1,000	100	23
BE1	Butoxyethanol	0	0	100	23
BE2	Butoxyethanol	45	0	100	37
BE3	Butoxyethanol	45	0	33	23
BE4	Butoxyethanol	45	0	100	23
BE5	Butoxyethanol	0	1,000	100	23

A.2.2 Instrumentation

Gas-phase measurements

A chemical ionization mass spectrometer (CIMS) was employed to monitor gas-phase analytes. The CIMS uses a Varian 1200 triple quadrupole mass analyzer to scan through masses from 50 to 350 amu. The masses are measured as a sum of the analyte mass and the reagent ion (either CF_3O^- or F^-). For further information on the selective chemistry with the CIMS reagent ions, see Crounse et al. 2006. While the CIMS is sensitive to quantifying the initial mixing ratios of both 2-BE and 2-EE, oxidation products in both systems correspond with the masses of the starting analytes thus complicating quantification of Δ2-BE and Δ2-EE reacted. Therefore, ethylene glycol was used as a tracer as detailed in the Results and Discussion section. Because the instruments sensitivity to the measured VOCs varied with ambient water vapor, and a humidity dependence correction was needed, the gas-phase analytes were normalized by the sum of the reagent ion signal (85 amu) and its cluster with water (103 amu), and H_2O_2 (119 amu).

A Fourier transform infrared (FTIR) spectrometer with a 19 cm path length was used to calibrate the CIMS sensitivity to 2-BE, 2-EE, and ethylene glycol. For calibrations, ppm-levels of the analytes were filled into an evacuated 0.5 L rounded bulb. The absolute concentration of the bulbs was calculated by comparing its measured FTIR spectrum to absorption cross sections from reference spectra provided by the Pacific Northwest National Laboratory (PNNL) database. Ozone produced during the high NO_x experiments was monitored using an APOA-360 Horiba ambient monitor. NO and NO_2 mixing ratios were measured using a Model T200 Teledyne nitrogen oxide analyzer. Humidity and temperature were monitored via a Vaisala HMM211 probe.

Particle-phase measurements

Aerosol number and size distribution were measured using a custom-built scanning mobility particle sizer (SMPS) which scanned from 35 to 600 nm. This SMPS is equipped with a TSI 3010 butanol-based condensation particle counter (CPC) and a TSI 3081 differential mobility analyzer (DMA). Aerosol sample is sent through an X-ray charge conditioner to give a known charge distribution. An average aerosol density of 1.4 g cm^{-3} was used to calculate the particle mass from the measured particle volume. An aerosol mass spectrometer (AMS) was used to determine the aerosol bulk chemical properties. The AMS uses a high-resolution time-of-flight (HR ToF) mass spectrometer which was run in V-mode. O:C ratios were derived through Squirrel (1.571) and Pika (1.161) high-resolution toolkits.

The mixing ratio of OH in the reactors was inferred by using the rate coefficient of the tracer, ethylene glycol, with OH, (1.47 ± 0.26) x 10^{-11} cm^{-3} mol^{-1} s^{-1} (Aschmann et al., 1998). The reaction rate of ethylene glycol was also monitored, along with the formation of its primary oxidation product, glycoaldehyde:

$$HOCH_2CH_2OH \xrightarrow{OH,O_2} HOCH_2CHO + H_2O + HO_2$$

We assumed the k_{OH} of 2-butoxyethanol (2-BE) and 2-ethoxyethanol (2-EE) to be (2.94 ± 0.43) x 10^{-11} and (1.94 ± 0.2) x 10^{-11} cm^3 $molecule^{-1}$ s^{-1}, respectively (Stemmler et al., 1996 and Aschmann et al., 1998). Using the inferred OH mixing ratio and the kinetic rate constants, Δ2-BE and Δ2-EE were calculated.

$$[OH] = -k_{OH\,(tracer)}[tracer]$$

$$VOC = \frac{\partial [VOC]}{\partial t} \frac{-1}{k_{OH\,(VOC)}[OH]}$$

$$\Delta VOC = VOC_{initial} - VOC_{final}$$

A3. Results and discussion

A3.1 SOA yield correlated to peroxy radical bimolecular lifetime in ethoxyethanol system

Ethoxyethanol (2-EE) SOA yields ranged from 4.5 – 22%. These values correlated well with the bimolecular lifetime of the of the 2-EE peroxy radical (τ_{RO2}).

The 2-EE peroxy radical (which we will denote here simply as RO_2), has four major pathways for reaction; it can react unimolecularly or with NO, RO_2, or HO_2. The NO pathway primarily leads to alkoxy radical formation and the formation of nitrates (RNO_2). The RO_2 + RO_2 self-reaction leads to the formation of alkoxy radicals and compounds with hydroxy terminal groups. Peroxy reaction with HO_2 can often lead to compounds with carbonyl, hydroxy, and hydroperoxyl functional groups.

The unimolecular pathway, also known as autoxidation, typically occurs in low NO conditions (e.g., [NO] < 500 ppt) (Crounse et al., 2013). The autoxidation mechanism involves an intermolecular and intramolecular H-shift in peroxy radicals. This reactive pathway typically leads to ketone hydroperoxide products. Recently, 2-EE was shown to readily autoxidize under typical ambient conditions (Yu et al., 2023).

The typical lifetime of RO_2 (τ_{RO2}) is >10s for a typical summer urban atmosphere. The fate of the RO_2 radical depends on the τ_{RO2}. For example, when NO levels are ≤ 100 ppt, peroxy radical lifetimes are 10 – 100s, long enough for the autoxidation pathway to be competitive with HO_2, NO, and RO_2 reaction pathways.

The correlation between τ_{RO2} and SOA yields is reported in Table A2 and Figure A1. For bimolecular lifetimes << 1 s, the SOA Y < 10%. This is congruent with past studies of 2-EE SOA formation in the presence of NO_x and H_2O_2 (Yu et al., 2023).

Table A2: Results from ethoxyethanol experiments. These yields have accounted for vapor wall losses.

Experiment	τ_{RO2} (s)	SOA Yield
EE1	1	13%
EE2	20 (high temp)	14%
EE3	20	22%
EE4	7	14%
EE5	0.005	4.5%

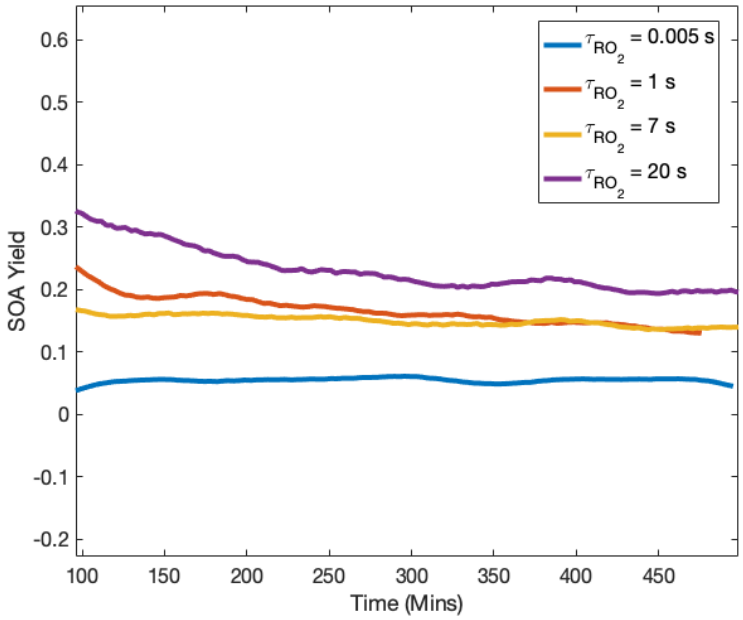

Figure A1: SOA yields from ethoxyethanol oxidation are correlated with bimolecular lifetimes.

For short τ_{RO2} where NO is present, products such as ethoxy-nitrate were observed, as illustrated in Figure A2. We were, however, unable to confirm the presence of the hydroperoxyl nitrate product, similar to past work (Yu et al., 2023). Though it appears some NO-products formed, given the relatively low SOA yield, it may be that the nitrate products led to fragmentation. Similar to past work, we observed the formation of 2-OH-ethylformate, a C3 product that forms under high-NO conditions (Yu et al., 2023). Others have also proposed several fragmentation products in the NO oxidative pathway of 2-EE, such as formaldehyde, glycolaldehyde, and acetaldehyde (Colmenar et al., 2020).

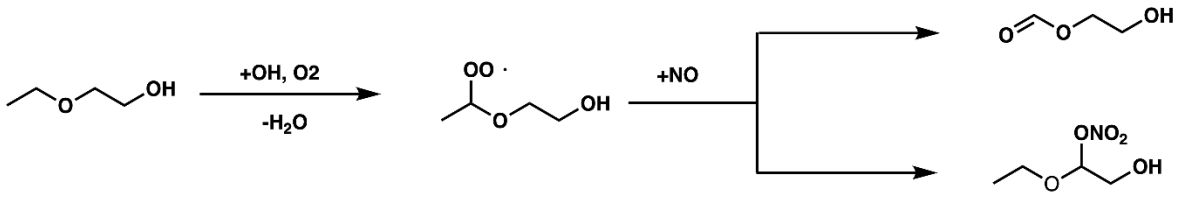

Figure A2: When NO dominates, some hydroxynitrate product may form but it appears that 2-OH-ethylformate forms significantly (Yu et al., 2023).

HO_2 pathways led to the formation of an ethoxyethanol ketone product (EE=O) and significant amounts of ethoxyethanol hydroperoxide (EE-OOH) (Figure A3). RO_2 + RO_2 can similarly lead to the formation of EE=O. We also observed the RO_2 product hydroxy-EE (EE-OH).

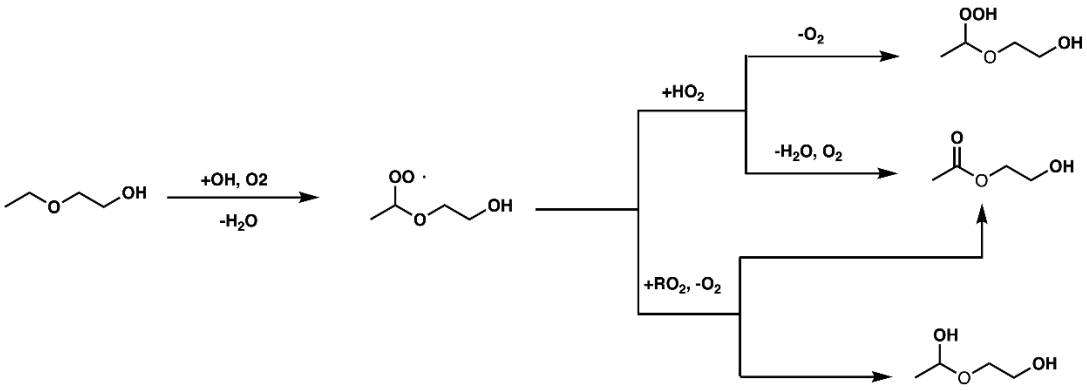

Figure A3: HO_2 and RO_2 pathways for ethoxyethanol photooxidation.

These high O:C ratio photooxidation products illustrate how greater amounts of SOA are likely formed in lower NO conditions, where the RO_2 react primarily with HO_2 or undergo H-shift chemistry compared to high-NO conditions, where the RO_2 react primarily with NO.

If the bimolecular lifetime is sufficiently long, the peroxy radical intermediate can undergo a 1,5 H-shift to form a peroxy hydroperoxyl radical intermediate (OO-EE-OOH). This radical intermediate can then undergo additional HO_2 chemistry. We observed the formation of a hydroperoxyl ketone product that likely forms as a result of HO_2 reaction with the OO-EE-OOH intermediate (Figure A4). However, we did not observe the di-hydroperoxy product proposed in past work (Yu et al., 2023).

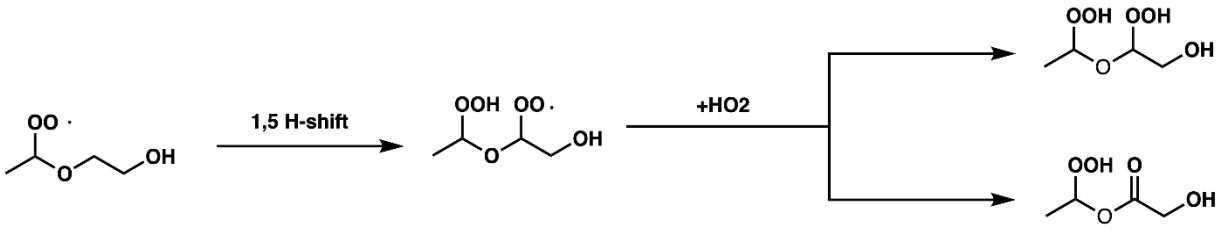

Figure A4: HO_2 can react with the hydroperoxide peroxy radical to form additional oxygenated products. Note that we do not observe the di-hydroperoxy product.

The SOA yield (Y) reached > 20% when bimolecular lifetimes are ~20 s. In this chemical regime, >30% of RO_2 formed are estimated to undergo an H-shift. We observed the formation of one such H-shift product, the hydroperoxyl ketone (OOH-EE=O) as illustrated in Figure A5. We observed very little to no gas-phase

formation of the di-hydroperoxy aldehyde (OOH-EE-CHO), the hydroperoxyl hydroxy ketone (oxo-EE-ROOH), or epoxide products also illustrated in Figure A5. This does not necessarily preclude their existence as it may be due to insufficient sensitivity of the CIMS.

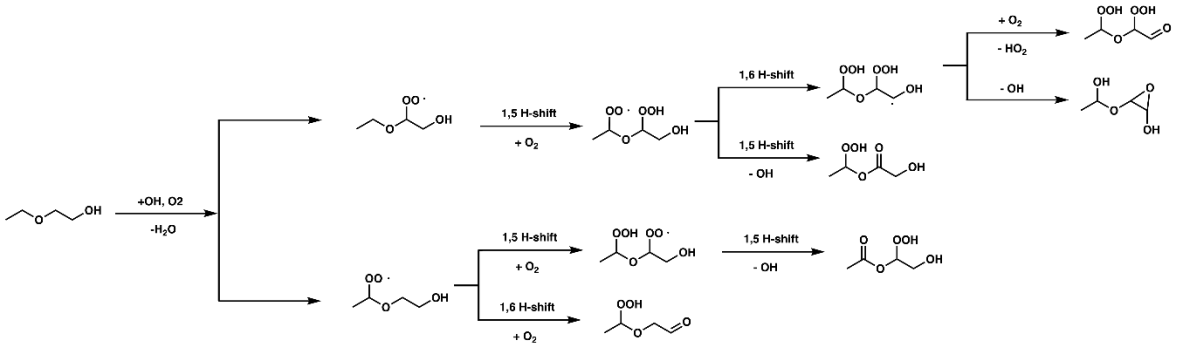

Figure A5: Autoxidation chemistry of 2-EE.

Experiment EE2 had a comparable bimolecular lifetime to that of EE3 but was conducted at a higher temperature (10 degrees warmer). The hydrogen shifts reaction rates with RO_2 can occur faster at higher temperatures (Praske et al., 2018). We found, however, that the SOA yield rate was lower at ~10°C higher temperature: 14%. Despite autoxidation products forming at faster rates, the higher temperatures led to reduced partition into the particle phase. It may be that in experiment EE2 the temperature effects out-competed the kinetics in SOA formation. For experiments EE1, EE3–EE5, O:C ratios from the analyzed AMS data are presented in Figure A6. We found that for experiments EE3 (τ_{RO2} = 20s) and EE4 (τ_{RO2} = 7s), the O:C ratios are higher than for experiments EE1 (τ_{RO2} = 1s) and E5 (τ_{RO2} = 0.005s). This is congruent with the hypothesis that highly oxygenated organic molecules formed from autoxidation pathways contribute to higher SOA yields in experiments with longer bimolecular lifetimes. Note that the duration of experiment EE3 was much longer than that of the other experiments because the amount of irradiation used in this experiment was less. However, a similar amount of hydrocarbon was reacted as in experiments E1, E4, and E5.

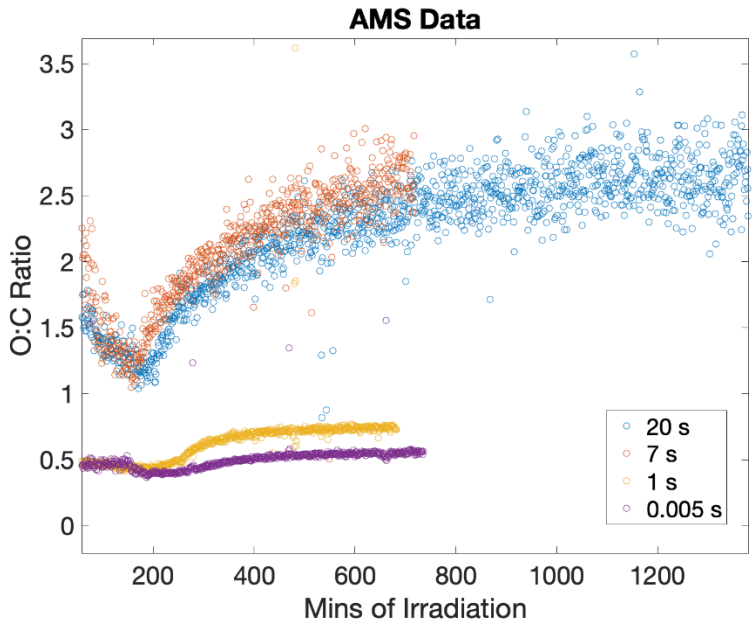

Figure A6: AMS data for experiments EE1 (τ_{RO2} = 1s), EE3 (τ_{RO2}= 20s), EE4 (τ_{RO2} = 7s) and EE5 (τ_{RO2} = 0.005s). The first hour of data is omitted because a significant amount of organic aerosol has yet to form during this time. For reference, **τ_{RO2} is approximately** 7s at [NO] = 0.5 ppb.

A3.2 Butoxyethanol chemistry may lead to more fragmentation

SOA yields of butoxyethanol (2-BE) range from 1 – 6% (Table A3). Unlike in the 2-EE, SOA yield for 2-BE did not appear to correlate with τ_{RO2}.

Table A3: Results of butoxyethanol experiments.

Experiment	τ_{RO2} (s)	SOA Yield
BE1	1	5%
BE2	20 (high temp)	1%
BE3	20	6%
BE4	7	2%
BE5	0.005	5%

The lack of correlation between SOA yield and peroxy radical bimolecular lifetime may be an indicator that different mechanisms dominate in the 2-BE system. Stemmler et al. (1997) suggested that with greater than four carbons present, the alkoxy radical of 2-BE may decompose via an isomerization reaction in high NO conditions. They observed ethyl formate (43± 5)% and ethylene glycol monoformate (36± 7)% account for a large yield of all butoxyethanol + OH products in high NO conditions. Ethyl formate and ethylene glycol monoformate were observed in our study but were left unquantified due to challenges with calibrating the absolute sensitivities of these compounds to our instrumentation. The present work also recognizes the formation of organic nitrates though we estimated yields in smaller quantities. This is congruent with past work in Yu et al., (2023).

Because of the oxygen-containing functional groups on these glycol ether compounds, such as the terminal OH group and ether linkage (Crounse et al., 2013), at higher bimolecular lifetimes, we hypothesized that the 2-EE forms autoxidation products, including an epoxide, with sufficiently low volatilities to partition to SOA. The hydroxyl group stabilizes the radical intermediate while the ether linkage can activate the C-H bond and lower the energy barrier for hydrogen abstraction. Given that the SOA yields of 2-BE remained low even at higher bimolecular lifetimes, it is reasonable to hypothesize that different oxidation products formed compared to 2-EE. Given the nearly identical chemical structure between 2-EE and 2-BE, this comes as a surprise.

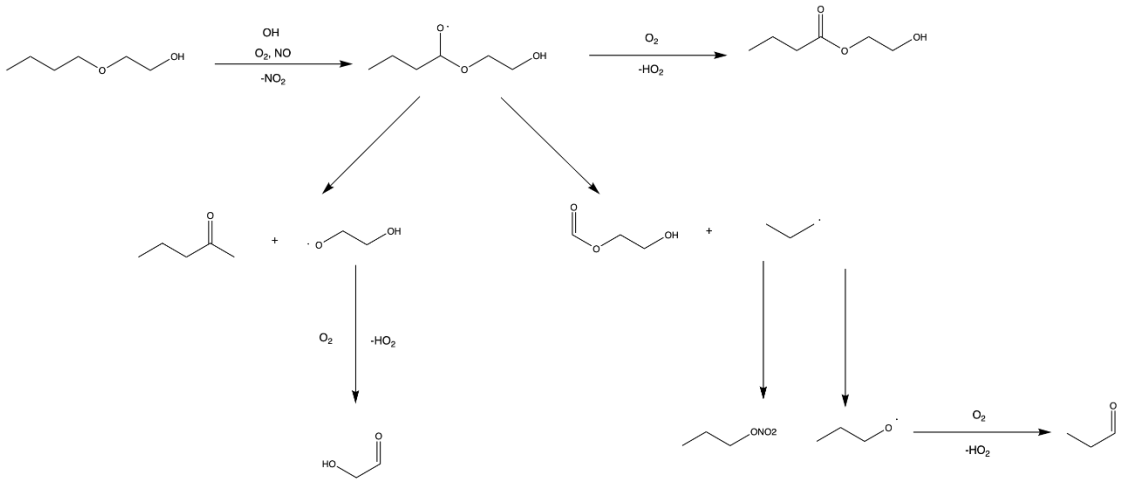

Figure A7: Butoxyethanol oxidation proposed by Stemmler et al. (1997) which illustrates potential fragmentation formation. Note that only one isomer is shown though several peroxy and subsequent alkoxy radicals are likely to form, excepting H-abstraction from the hydroxyl group and methyl groups.

Stemmler et al. (1997) showed that 2-BE can readily isomerize, typically from an alkoxy radical intermediate (Figure A7). Because of the experiments in the study were done in low NO conditions, it is possible that isomerization occurs from a peroxy radical intermediate. It is possible that instead of forming the hypothesized peroxide, isomerization instead occurs, leading to fragmentation. It may be that for a C_6 compound like 2-BE, the formation of a 5-member or 6 -member ring is more favorable than the sterically-hindered epoxide. After decomposition, the resulting close-shelled product could be a C_3 compound and thus have lower volatility. For example, CIMS data showed significant formation for a product at m/z = 175, corresponding to the molecular weight of ethylene glycol monoformate (MW = 90). Further studies are needed to confirm the complete mechanism of 2-BE at $\tau_{RO2} =$ 10 s.

A4. References

Aschmann, S.M.; Atkinson, R. Kinetics of the Gas-Phase Reactions of the OH Radical with Selected Glycol Ethers, Glycols, and Alcohols. International Journal of Chemical Kinetics 1998, 30, 533 – 540.

Burnett, R.; Chen, H.; Szyszkowicz, M.; Fann, N.; Hubbell, B.; Pope, C. A.; Apte, J. S.; Brauer, M.; Cohen, A.; Weichenthal, S.; Coggins, J.; Di, Q.; Brunekreef, B.; Frostad, J.; Lim, S. S.; Kan, H.; Walker, K. D.; Thurston, G. D.; Hayes, R. B.; Lim, C. C.; Turner, M. C.; Jerrett, M.; Krewski, D.; Gapstur, S. M.; Diver, W. R.; Ostro, B.; Goldberg, D.; Crouse, D. L.; Martin, R. V.; Peters, P.; Pinault, L.; Tjepkema, M.; Donkelaar, A. van; Villeneuve, P. J.; Miller, A. B.; Yin, P.; Zhou, M.; Wang, L.; Janssen, N. A. H.; Marra, M.; Atkinson, R. W.; Tsang, H.; Thach, T. Q.; Cannon, J. B.; Allen, R. T.; Hart, J. E.; Laden, F.; Cesaroni, G.; Forastiere, F.; Weinmayr, G.; Jaensch, A.; Nagel, G.; Concin, H.; Spadaro, J. V. Global Estimates of Mortality Associated with Long-Term Exposure to Outdoor Fine Particulate Matter. PNAS 2018, 115 (38), 9592–9597. https://doi.org/10.1073/pnas.1803222115.

California Air Resources Board (CARB), Low-Emission Vehicle Program, Accessed at: https://ww2.arb.ca.gov/our-work/programs/low-emission-vehicle-program. Last accessed: Feb. 7, 2022

California Emissions Projections Analysis Model (CEPAM) 2019 v1.03. Accessed at: https://ww2.arb.ca.gov/applications/cepam2019v103-standard-emission-tool. Last accessed: Feb 7, 2022.

Chan, A. W. H.; Kautzman, K. E.; Chhabra, P. S.; Surratt, J. D.; Chan, M. N.; Crounse, J. D.; Kürten, A.; Wennberg, P. O.; Flagan, R. C.; Seinfeld, J. H. Secondary Organic Aerosol Formation from Photooxidation of Naphthalene and Alkylnaphthalenes: Implications for Oxidation of Intermediate Volatility Organic Compounds (IVOCs). Atmospheric Chemistry and Physics 2009, 9 (9), 3049–3060. https://doi.org/10.5194/acp-9-3049-2009

Chow, J. C.; Watson, J. G.; Lowenthal, D. H.; Magliano, K. L. Loss of PM2.5 Nitrate from Filter Samples in Central California. Journal of the Air & Waste Management Association 2005, 55 (8), 1158–1168. https://doi.org/10.1080/10473289.2005.10464704

Cocker, D.R.; Li, L.; Prince, J.D.; Kacarab, M.; Chen, C.L. Review of VOC Emissions Inventory for Consumer Products and Architectural Coatings for Potential Alternative Fate and Availability Corrections. Consumer Specialty Products Association Report 2014.

Cohen, A. J.; Brauer, M.; Burnett, R.; Anderson, H. R.; Frostad, J.; Estep, K.; Balakrishnan, K.; Brunekreef, B.; Dandona, L.; Dandona, R.; Feigin, V.; Freedman, G.; Hubbell, B.; Jobling, A.; Kan, H.; Knibbs, L.; Liu, Y.; Martin, R.; Morawska, L.; Pope, C. A.; Shin, H.; Straif, K.; Shaddick, G.; Thomas, M.; van Dingenen, R.; van Donkelaar, A.; Vos, T.; Murray, C. J. L.; Forouzanfar, M. H. Estimates and 25-Year

Trends of the Global Burden of Disease Attributable to Ambient Air Pollution: An Analysis of Data from the Global Burden of Diseases Study 2015. Lancet 2017, 389 (10082), 1907–1918. https://doi.org/10.1016/S0140-6736(17)30505-6.

Colmenar, I.; Salgado, S.; Martin, P.; Aranda, I.; Tapia, A.; Cabanas, B. Tropospheric Reactivity of 2-Ethoxyethanol with OH and NO_3 Radicals and Cl atoms: Kinetic and Mechanistic Study. Atmospheric Environment 2020, 224, 117367.

Crounse, J.D.; Nielsen, L.B.; Jorgensen, S.; Kjaergaard, H.G.; Wennberg, P.O. Autoxidation of Organic Compounds in the Atmosphere. The Journal of Physical Chemistry Letters 2013, 4, 3513 – 3520.

Docherty, K. S.; Aiken, A. C.; Huffman, J. A.; Ulbrich, I. M.; DeCarlo, P. F.; Sueper, D.; Worsnop, D. R.; Snyder, D. C.; Peltier, R. E.; Weber, R. J.; Grover, B. D.; Eatough, D. J.; Williams, B. J.; Goldstein, A. H.; Ziemann, P. J.; Jimenez, J. L. The 2005 Study of Organic Aerosols at Riverside (SOAR-1): Instrumental Intercomparisons and Fine Particle Composition. Atmospheric Chemistry and Physics 2011, 11 (23), 12387–12420. https://doi.org/10.5194/acp-11-12387-2011.

Dzepina, K.; Volkamer, R. M.; Madronich, S.; Tulet, P.; Ulbrich, I. M.; Zhang, Q.; Cappa, C. D.; Ziemann, P. J.; Jimenez, J. L. Evaluation of Recently-Proposed Secondary Organic Aerosol Models for a Case Study in Mexico City. Atmospheric Chemistry and Physics 2009, 9 (15), 5681–5709. https://doi.org/10.5194/acp-9-5681-2009

Ellis, R. A.; Murphy, J. G.; Pattey, E.; van Haarlem, R.; O'Brien, J. M.; Herndon, S. C. Characterizing a Quantum Cascade Tunable Infrared Laser Differential Absorption Spectrometer (QC-TILDAS) for Measurements of Atmospheric Ammonia. Atmospheric Measurement Techniques 2010, 3 (2), 397–406. https://doi.org/10.5194/amt-3-397-2010

Ensberg, J. J.; Craven, J. S.; Metcalf, A. R.; Allan, J. D.; Angevine, W. M.; Bahreini, R.; Brioude, J.; Cai, C.; Coe, H.; Gouw, J. A. de; Ellis, R. A.; Flynn, J. H.; Haman, C. L.; Hayes, P. L.; Jimenez, J. L.; Lefer, B. L.; Middlebrook, A. M.; Murphy, J. G.; Neuman, J. A.; Nowak, J. B.; Roberts, J. M.; Stutz, J.; Taylor, J. W.; Veres, P. R.; Walker, J. M.; Seinfeld, J. H. Inorganic and Black Carbon Aerosols in the Los Angeles Basin during CalNex. Journal of Geophysical Research: Atmospheres 2013, 118 (4), 1777–1803. https://doi.org/10.1029/2012JD018136.

Ensberg, J. J.; Hayes, P. L.; Jimenez, J. L.; Gilman, J. B.; Kuster, W. C.; de Gouw, J. A.; Holloway, J. S.; Gordon, T. D.; Jathar, S.; Robinson, A. L.; Seinfeld, J. H. Emission Factor Ratios, SOA Mass Yields, and the Impact of Vehicular Emissions on SOA Formation. Atmospheric Chemistry and Physics 2014, 14 (5), 2383–2397. https://doi.org/10.5194/acp-14-2383-2014.

Environmental Protection Agency (EPA), Glycol Ethers (2016). Accessed at: https://www.epa.gov/sites/default/files/2016-09/documents/glycol-ethers.pdf. Last accessed: July 2024.

Environmental Protection Agency (EPA), PM-2.5 (2012) Designated Area/State Information, Accessed at: https://www3.epa.gov/airquality/greenbook/kbtc.html. Last accessed: Feb. 23, 2022

Environmental Protection Agency (EPA), Regulations for On-road Vehicles and Engines, Accessed at: https://www.epa.gov/regulations-emissions-vehicles-and-engines/regulations-onroad-vehicles-and-engines. Last accessed: Feb 7, 2022.

Fountoukis, C.; Nenes, A. ISORROPIA II: A Computationally Efficient Thermodynamic Equilibrium Model for K^+;Ca^{2+};Mg^{2+};NH_4^+;Na^+;SO_4^{2-};NO_3^-;Cl^- ;H_2O Aerosols. Atmospheric Chemistry and Physics 2007, 7 (17), 4639–4659. https://doi.org/10.5194/acp-7-4639-2007

Gentner, D. R.; Jathar, S. H.; Gordon, T. D.; Bahreini, R.; Day, D. A.; El Haddad, I.; Hayes, P. L.; Pieber, S. M.; Platt, S. M.; de Gouw, J.; Goldstein, A. H.; Harley, R. A.; Jimenez, J. L.; Prévôt, A. S. H.; Robinson, A. L. Review of Urban Secondary Organic Aerosol Formation from Gasoline and Diesel Motor Vehicle Emissions. Environ. Sci. Technol. 2017, 51 (3), 1074–1093. https://doi.org/10.1021/acs.est.6b04509.

Gordon, T. D.; Presto, A. A.; May, A. A.; Nguyen, N. T.; Lipsky, E. M.; Donahue, N. M.; Gutierrez, A.; Zhang, M.; Maddox, C.; Rieger, P.; Chattopadhyay, S.; Maldonado, H.; Maricq, M. M.; Robinson, A. L. Secondary Organic Aerosol Formation Exceeds Primary Particulate Matter Emissions for Light-Duty Gasoline Vehicles. Atmospheric Chemistry and Physics 2014, 14 (9), 4661–4678. https://doi.org/10.5194/acp-14-4661-2014.

Griffith, S. M.; Hansen, R. F.; Dusanter, S.; Michoud, V.; Gilman, J. B.; Kuster, W. C.; Veres, P. R.; Graus, M.; Gouw, J. A. de; Roberts, J.; Young, C.; Washenfelder, R.; Brown, S. S.; Thalman, R.; Waxman, E.; Volkamer, R.; Tsai, C.; Stutz, J.; Flynn, J. H.; Grossberg, N.; Lefer, B.; Alvarez, S. L.; Rappenglueck, B.; Mielke, L. H.; Osthoff, H. D.; Stevens, P. S. Measurements of Hydroxyl and Hydroperoxy Radicals during CalNex-LA: Model Comparisons and Radical Budgets. Journal of Geophysical Research: Atmospheres 2016, 121 (8), 4211–4232. https://doi.org/10.1002/2015JD024358

Guo, H.; Liu, J.; Froyd, K. D.; Roberts, J. M.; Veres, P. R.; Hayes, P. L.; Jimenez, J. L.; Nenes, A.; Weber, R. J. Fine Particle PH and Gas–Particle Phase Partitioning of Inorganic Species in Pasadena, California, during the 2010 CalNex Campaign. Atmospheric Chemistry and Physics 2017, 17 (9), 5703–5719. https://doi.org/10.5194/acp-17-5703-2017

Hasheminassab, S.; Daher, N.; Ostro, B. D.; Sioutas, C. Long-Term Source Apportionment of Ambient Fine Particulate Matter (PM2.5) in the Los Angeles Basin: A Focus on Emissions Reduction from Vehicular Sources. Environmental Pollution 2014, 193, 54–64. https://doi.org/10.1016/j.envpol.2014.06.012

Hayes, P. L.; Ortega, A. M.; Cubison, M. J.; Froyd, K. D.; Zhao, Y.; Cliff, S. S.; Hu, W. W.; Toohey, D. W.; Flynn, J. H.; Lefer, B. L.; Grossberg, N.; Alvarez, S.; Rappenglück, B.; Taylor, J. W.; Allan, J. D.; Holloway, J. S.; Gilman, J. B.; Kuster, W. C.; de Gouw, J. A.; Massoli, P.; Zhang, X.; Liu, J.; Weber, R. J.; Corrigan, A. L.; Russell, L. M.; Isaacman, G.; Worton, D. R.; Kreisberg, N. M.; Goldstein, A. H.; Thalman, R.; Waxman, E. M.; Volkamer, R.; Lin, Y. H.; Surratt, J. D.; Kleindienst, T. E.; Offenberg, J. H.; Dusanter, S.; Griffith, S.; Stevens, P. S.; Brioude, J.; Angevine, W. M.; Jimenez, J. L. Organic Aerosol Composition and Sources in Pasadena, California, during the 2010 CalNex Campaign. J. Geophys. Res. Atmos. 2013, 118 (16), 9233–9257. https://doi.org/10.1002/jgrd.50530

Hayes, P. L.; Carlton, A. G.; Baker, K. R.; Ahmadov, R.; Washenfelder, R. A.; Alvarez, S.; Rappenglück, B.; Gilman, J. B.; Kuster, W. C.; de Gouw, J. A.; Zotter, P.; Prévôt, A. S. H.; Szidat, S.; Kleindienst, T. E.; Offenberg, J. H.; Ma, P. K.; Jimenez, J. L. Modeling the Formation and Aging of Secondary Organic Aerosols in Los Angeles during CalNex 2010. Atmospheric Chemistry and Physics 2015, 15 (10), 5773–5801. https://doi.org/10.5194/acp-15-5773-2015.

Heald, C. L.; Collett, J. L. J.; Lee, T.; Benedict, K. B.; Schwandner, F. M.; Li, Y.; Clarisse, L.; Hurtmans, D. R.; Van Damme, M.; Clerbaux, C.; Coheur, P.-F.; Philip, S.; Martin, R. V.; Pye, H. O. T. Atmospheric Ammonia and Particulate Inorganic Nitrogen over the United States. Atmospheric Chemistry and Physics 2012, 12 (21), 10295–10312. https://doi.org/10.5194/acp-12-10295-2012.

Hering, S.; Cass, G. The Magnitude of Bias in the Measurement of PM $_{25}$ Arising from Volatilization of Particulate Nitrate from Teflon Filters. Journal of the Air & Waste Management Association 1999, 49 (6), 725–733. https://doi.org/10.1080/10473289.1999.10463843

Jathar, S. H.; Gordon, T. D.; Hennigan, C. J.; Pye, H. O. T.; Pouliot, G.; Adams, P. J.; Donahue, N. M.; Robinson, A. L. Unspeciated Organic Emissions from Combustion Sources and Their Influence on the Secondary Organic Aerosol Budget in the United States. PNAS 2014, 111 (29), 10473–10478. https://doi.org/10.1073/pnas.1323740111.

Khare, P.; Gentner, D. R. Considering the Future of Anthropogenic Gas-Phase Organic Compound Emissions and the Increasing Influence of Non-Combustion Sources on Urban Air Quality. Atmospheric Chemistry and Physics 2018, 18 (8), 5391–5413. https://doi.org/10.5194/acp-18-5391-2018.

Khare, P.; Machesky, J.; Soto, R.; He, M.; Presto, A. A.; Gentner, D. R. Asphalt-Related Emissions Are a Major Missing Nontraditional Source of Secondary Organic Aerosol Precursors. Science Advances 2020, 6 (36), eabb9785. https://doi.org/10.1126/sciadv.abb9785.

Kim, B. M.; Cassmassi, J.; Hogo, H.; Zeldin, M. D. Positive Organic Carbon Artifacts on Filter Medium During PM2.5 Sampling in the South Coast Air Basin. Aerosol Science and Technology 2001, 34 (1), 35–41. https://doi.org/10.1080/02786820118227.

Lawson, D. R. The Southern California Air Quality Study. Journal of the Air & Waste Management Association 1990, 40 (2), 156–165. https://doi.org/10.1080/10473289.1990.10466671

Le, T.-C.; Shukla, K. K.; Chen, Y.-T.; Chang, S.-C.; Lin, T.-Y.; Li, Z.; Pui, D. Y. H.; Tsai, C.-J. On the Concentration Differences between PM2.5 FEM Monitors and FRM Samplers. Atmospheric Environment 2020, 222, 117138. https://doi.org/10.1016/j.atmosenv.2019.117138.

Liu, C.-N.; Lin, S.-F.; Tsai, C.-J.; Wu, Y.-C.; Chen, C.-F. Theoretical Model for the Evaporation Loss of PM2.5 during Filter Sampling. Atmospheric Environment 2015, 109, 79–86. https://doi.org/10.1016/j.atmosenv.2015.03.012.

Liu, C.-N.; Awasthi, A.; Hung, Y.-H.; Gugamsetty, B.; Tsai, C.-J.; Wu, Y.-C.; Chen, C.-F. Differences in 24-h Average PM2.5 Concentrations between the Beta Attenuation Monitor (BAM) and the Dichotomous Sampler (Dichot). Atmospheric Environment 2013, 75, 341–347. https://doi.org/10.1016/j.atmosenv.2013.04.062.

Ma, P. K.; Zhao, Y.; Robinson, A. L.; Worton, D. R.; Goldstein, A. H.; Ortega, A. M.; Jimenez, J. L.; Zotter, P.; Prévôt, A. S. H.; Szidat, S.; Hayes, P. L. Evaluating the Impact of New Observational Constraints on P-S/IVOC Emissions, Multi-Generation Oxidation, and Chamber Wall Losses on SOA Modeling for Los Angeles, CA. Atmospheric Chemistry and Physics 2017, 17 (15), 9237–9259. https://doi.org/10.5194/acp-17-9237-2017.

McDonald, B. C.; Goldstein, A. H.; Harley, R. A. Long-Term Trends in California Mobile Source Emissions and Ambient Concentrations of Black Carbon and Organic Aerosol. Environ. Sci. Technol. 2015, 49 (8), 5178–5188. https://doi.org/10.1021/es505912b.

McDonald, B. C.; Gouw, J. A. de; Gilman, J. B.; Jathar, S. H.; Akherati, A.; Cappa, C. D.; Jimenez, J. L.; Lee-Taylor, J.; Hayes, P. L.; McKeen, S. A.; Cui, Y. Y.; Kim, S.-W.; Gentner, D. R.; Isaacman-VanWertz, G.; Goldstein, A. H.; Harley, R. A.; Frost, G. J.; Roberts, J. M.; Ryerson, T. B.; Trainer, M. Volatile Chemical Products Emerging as Largest Petrochemical Source of Urban Organic Emissions. Science 2018, 359 (6377), 760–764. https://doi.org/10.1126/science.aaq0524.

Middlebrook, A. M.; Bahreini, R.; Jimenez, J. L.; Canagaratna, M. R. Evaluation of Composition-Dependent Collection Efficiencies for the Aerodyne Aerosol Mass Spectrometer Using Field Data. Aerosol Science and Technology 2012, 46 (3), 258–271. https://doi.org/10.1080/02786826.2011.620041.

Mielke, L. H.; Stutz, J.; Tsai, C.; Hurlock, S. C.; Roberts, J. M.; Veres, P. R.; Froyd, K. D.; Hayes, P. L.; Cubison, M. J.; Jimenez, J. L.; Washenfelder, R. A.; Young, C. J.; Gilman, J. B.; Gouw, J. A. de; Flynn, J. H.; Grossberg, N.; Lefer, B. L.; Liu, J.; Weber, R. J.; Osthoff, H. D. Heterogeneous Formation of Nitryl Chloride and Its Role as a Nocturnal NOx Reservoir Species during CalNex-LA 2010. Journal of Geophysical Research: Atmospheres 2013, 118 (18), 10,638-10,652. https://doi.org/10.1002/jgrd.50783.

Ng, N. L.; Kroll, J. H.; Chan, A. W. H.; Chhabra, P. S.; Flagan, R. C.; Seinfeld, J. H. Secondary Organic Aerosol Formation from m-Xylene, Toluene, and Benzene. Atmospheric Chemistry and Physics 2007, 7 (14), 3909–3922. https://doi.org/10.5194/acp-7-3909-2007.

Ortega, A. M.; Hayes, P. L.; Peng, Z.; Palm, B. B.; Hu, W.; Day, D. A.; Li, R.; Cubison, M. J.; Brune, W. H.; Graus, M.; Warneke, C.; Gilman, J. B.; Kuster, W. C.; Gouw, J. de; Gutiérrez-Montes, C.; Jimenez, J. L. Real-Time Measurements of Secondary Organic Aerosol Formation and Aging from Ambient Air in an Oxidation Flow Reactor in the Los Angeles Area. Atmospheric Chemistry and Physics 2016, 16 (11), 7411–7433. https://doi.org/10.5194/acp-16-7411-2016.

Paatero, P.; Tapper, U. Positive Matrix Factorization: A Non-Negative Factor Model with Optimal Utilization of Error Estimates of Data Values. Environmetrics 1994, 5 (2), 111–126. https://doi.org/10.1002/env.3170050203.

Parrish, D. D.; Stohl, A.; Forster, C.; Atlas, E. L.; Blake, D. R.; Goldan, P. D.; Kuster, W. C.; Gouw, J. A. de. Effects of Mixing on Evolution of Hydrocarbon Ratios in the Troposphere. Journal of Geophysical Research: Atmospheres 2007, 112 (D10). https://doi.org/10.1029/2006JD007583.

Pennington, E. A.; Seltzer, K. M.; Murphy, B. N.; Qin, M.; Seinfeld, J. H.; Pye, H. O. T. Modeling Secondary Organic Aerosol Formation from Volatile Chemical Products. Atmospheric Chemistry and Physics Discussions 2021, 1–26. https://doi.org/10.5194/acp-2021-547.

Pollack, I. B.; Ryerson, T. B.; Trainer, M.; Parrish, D. D.; Andrews, A. E.; Atlas, E. L.; Blake, D. R.; Brown, S. S.; Commane, R.; Daube, B. C.; Gouw, J. A. de; Dubé, W. P.; Flynn, J.; Frost, G. J.; Gilman, J. B.; Grossberg, N.; Holloway, J. S.; Kofler, J.; Kort, E. A.; Kuster, W. C.; Lang, P. M.; Lefer, B.; Lueb, R. A.; Neuman, J. A.; Nowak, J. B.; Novelli, P. C.; Peischl, J.; Perring, A. E.; Roberts, J. M.; Santoni, G.; Schwarz, J. P.; Spackman, J. R.; Wagner, N. L.; Warneke, C.; Washenfelder, R. A.; Wofsy, S. C.; Xiang, B. Airborne and Ground-Based Observations of a Weekend Effect in Ozone, Precursors, and Oxidation Products in the

California South Coast Air Basin. Journal of Geophysical Research: Atmospheres 2012, 117 (D21). https://doi.org/10.1029/2011JD016772.

Pollack, I. B.; Ryerson, T. B.; Trainer, M.; Neuman, J. A.; Roberts, J. M.; Parrish, D. D. Trends in Ozone, Its Precursors, and Related Secondary Oxidation Products in Los Angeles, California: A Synthesis of Measurements from 1960 to 2010. Journal of Geophysical Research: Atmospheres 2013, 118 (11), 5893–5911. https://doi.org/10.1002/jgrd.50472.

Praske, E.; Otkjær, R. V.; Crounse, J. D.; Hethcox, J. C.; Stoltz, B. M.; Kjaergaard, H. G.; Wennberg, P. O. Atmospheric Autoxidation Is Increasingly Important in Urban and Suburban North America. PNAS 2018, 115 (1), 64–69. https://doi.org/10.1073/pnas.1715540115.

Pye, H. O. T.; Ward-Caviness, C. K.; Murphy, B. N.; Appel, K. W.; Seltzer, K. M. Secondary Organic Aerosol Association with Cardiorespiratory Disease Mortality in the United States. Nat Commun 2021, 12 (1), 7215. https://doi.org/10.1038/s41467-021-27484-1.

Schauer, J. J.; Rogge, W. F.; Hildemann, L. M.; Mazurek, M. A.; Cass, G. R.; Simoneit, B. R. T. Source Apportionment of Airborne Particulate Matter Using Organic Compounds as Tracers. Atmospheric Environment 1996, 30 (22), 3837–3855. https://doi.org/10.1016/1352-2310(96)00085-4.

Schiferl, L. D.; Heald, C. L.; Nowak, J. B.; Holloway, J. S.; Neuman, J. A.; Bahreini, R.; Pollack, I. B.; Ryerson, T. B.; Wiedinmyer, C.; Murphy, J. G. An Investigation of Ammonia and Inorganic Particulate Matter in California during the CalNex Campaign. Journal of Geophysical Research: Atmospheres 2014, 119 (4), 1883–1902. https://doi.org/10.1002/2013JD020765.

Seltzer, K. M.; Murphy, B. N.; Pennington, E. A.; Allen, C.; Talgo, K.; Pye, H. O. T. Volatile Chemical Product Enhancements to Criteria Pollutants in the United States. Environ. Sci. Technol. 2021. https://doi.org/10.1021/acs.est.1c04298.

Seltzer, K. M.; Pennington, E.; Rao, V.; Murphy, B. N.; Strum, M.; Isaacs, K. K.; Pye, H. O. T. Reactive Organic Carbon Emissions from Volatile Chemical Products. Atmospheric Chemistry and Physics 2021, 21 (6), 5079–5100. https://doi.org/10.5194/acp-21-5079-2021.

Singer, B.C.; Destaillats, H.; Hodgson, A.T.; Nazaroff, W.W. Cleaning Products and Air Fresheners: Emissions and Resulting Concentrations of Glycol Ethers and Terpenoids. Indoor Air 2006, 16, 179 – 191.

Stemmler, K.; Kinnison, D.J.; Kerr, J.A. Room Temperature Rate Coefficients for the Reactions of OH Radicals with Some Monoethylene Glycol Monoalkyl Ethers. The Journal of Physical Chemistry 1996, 100, 2114-2116.

Stemmler, K.; Mengon, W.; Kinnison, D.J.; Kerr, J.A. OH Radical-Initiated Oxidation of 2-Butoxyethanol Under Laboratory Conditions Related to the Troposphere: Product Studies and Proposed Mechanisms. Environmental Science & Technology 1997, 31, 1496-1504.

Stone, E. A.; Zhou, J.; Snyder, D. C.; Rutter, A. P.; Mieritz, M.; Schauer, J. J. A Comparison of Summertime Secondary Organic Aerosol Source Contributions at Contrasting Urban Locations. Environ. Sci. Technol. 2009, 43 (10), 3448–3454. https://doi.org/10.1021/es8025209.

Tkacik, D. S.; Lambe, A. T.; Jathar, S.; Li, X.; Presto, A. A.; Zhao, Y.; Blake, D.; Meinardi, S.; Jayne, J. T.; Croteau, P. L.; Robinson, A. L. Secondary Organic Aerosol Formation from In-Use Motor Vehicle Emissions Using a Potential Aerosol Mass Reactor. Environ. Sci. Technol. 2014, 48 (19), 11235–11242. https://doi.org/10.1021/es502239v.

Ulbrich, I. M.; Canagaratna, M. R.; Zhang, Q.; Worsnop, D. R.; Jimenez, J. L. Interpretation of Organic Components from Positive Matrix Factorization of Aerosol Mass Spectrometric Data. Atmospheric Chemistry and Physics 2009, 9 (9), 2891–2918. https://doi.org/10.5194/acp-9-2891-2009.

Van Rooy, P.; Tasnia, A.; Barletta, B.; Buenconsejo, R.; Crounse, J. D.; Kenseth, C. M.; Meinardi, S.; Murphy, S.; Parker, H.; Schulze, B.; Seinfeld, J. H.; Wennberg, P. O.; Blake, D. R.; Barsanti, K. C. Observations of Volatile Organic Compounds in the Los Angeles Basin during COVID-19. ACS Earth Space Chem. 2021, 5 (11), 3045–3055. https://doi.org/10.1021/acsearthspacechem.1c00248.

Vecchi, R.; Valli, G.; Fermo, P.; D'Alessandro, A.; Piazzalunga, A.; Bernardoni, V. Organic and Inorganic Sampling Artefacts Assessment. Atmospheric Environment 2009, 43 (10), 1713–1720. https://doi.org/10.1016/j.atmosenv.2008.12.016.

Veres, P.; Roberts, J. M.; Warneke, C.; Welsh-Bon, D.; Zahniser, M.; Herndon, S.; Fall, R.; de Gouw, J. Development of Negative-Ion Proton-Transfer Chemical-Ionization Mass Spectrometry (NI-PT-CIMS) for the Measurement of Gas-Phase Organic Acids in the Atmosphere. International Journal of Mass Spectrometry 2008, 274 (1), 48–55. https://doi.org/10.1016/j.ijms.2008.04.032.

Warneke, C.; Gouw, J. A. de; Edwards, P. M.; Holloway, J. S.; Gilman, J. B.; Kuster, W. C.; Graus, M.; Atlas, E.; Blake, D.; Gentner, D. R.; Goldstein, A. H.; Harley, R. A.; Alvarez, S.; Rappenglueck, B.; Trainer, M.; Parrish, D. D. Photochemical Aging of Volatile Organic Compounds in the Los Angeles Basin: Weekday-Weekend Effect. Journal of Geophysical Research: Atmospheres 2013, 118 (10), 5018–5028. https://doi.org/10.1002/jgrd.50423.

Watson, J. G.; Chow, J. C.; Lu, Z.; Fujita, E. M.; Lowenthal, D. H.; Lawson, D. R.; Ashbaugh, L. L. Chemical Mass Balance Source Apportionment of PM10 during the Southern California Air Quality Study. Aerosol Science and Technology 1994, 21 (1), 1–36. https://doi.org/10.1080/02786829408959693.

Yu, H; Moller, K.H.; Buenconsejo, R.S.; Crounse, J.D.; Kjargaard, H.G.; Wennberg, P.O. Atmospheric Photo-Oxidation of 2-Ethoxyethanol: Autoxidation Chemistry of Glycol Ethers. The Journal of Physical Chemistry A 2023, 127 (45), 9564 – 9579.

Zhang, Q.; Worsnop, D. R.; Canagaratna, M. R.; Jimenez, J. L. Hydrocarbon-like and Oxygenated Organic Aerosols in Pittsburgh: Insights into Sources and Processes of Organic Aerosols. Atmospheric Chemistry and Physics 2005, 5 (12), 3289–3311. https://doi.org/10.5194/acp-5-3289-2005.

Zhao, Y.; Saleh, R.; Saliba, G.; Presto, A. A.; Gordon, T. D.; Drozd, G. T.; Goldstein, A. H.; Donahue, N. M.; Robinson, A. L. Reducing Secondary Organic Aerosol Formation from Gasoline Vehicle Exhaust. PNAS 2017, 114 (27), 6984–6989. https://doi.org/10.1073/pnas.1620911114.

Part B: Data Analysis of Ammonium Nitrate in the California South Coast Air Basin

California Air Resources Board Contract Number 22RD015

B1. Introduction

The Los Angeles (LA) airshed is one of the most polluted urban air basins in the United States. LA County has failed to attain the EPA's 2012 NAAQS for PM2.5 (Particulate Matter less than 2.5 μm in diameter; 12 μg m^{-3} annual average) every year in the last decade, and PM levels have stagnated despite strides in reducing precursor emissions like NO_x (EPA, 2012). In 2024, the standard was strengthened to 9 μg m^{-3}, posing even more urgent regulatory pressure. A confluence of physical and anthropogenic phenomena primes the LA basin for poor air quality: a large population, geographic barriers for ventilation, and a variety of natural and anthropogenic sources of emissions, to name a few (Parrish et al. 2016). The PM in Los Angeles is largely produced by partitioning of gas phase chemicals produced in the atmosphere to the condensed phase (secondary PM). Further, the PM contains a variety of organic and inorganic constituents. Given the complicated processes that tie the emissions of volatile organic and inorganic compounds to the formation of secondary PM, determining the relative importance of these emission sources remains a challenge and clouds opportunities for abatement (Pennington et al. 2021; Hayes et al. 2013). Recent studies have focused on characterizing and apportioning the organic component of secondary aerosol (McDonald et al. 2018; Nussbaumer and Cohen 2021; Gu, Guenther, and Faiola 2021; Zhao et al. 2022; Pfannerstill et al. 2024) and have illustrated that efforts to reduce VOC emissions are required to meet regulatory PM. Standards. However, inorganic species (primarily secondary nitrate and sulfate) continue to contribute significantly to PM2.5 mass in Los Angeles and much of Southern California (Hasheminassab et al. 2014a).

Ammonium Nitrate ($NH_4^+ \cdot NO_3^-$) has long been identified as one of the key components of LA aerosol (Kleeman and Cass 2001; Hasheminassab et al. 2014a). The particulate nitrate is produced from the co-partitioning of nitric acid (HNO_3) with ammonia (NH_3). HNO_3 forms in the atmosphere from nitrogen oxides (NO_x), whose source is overwhelmingly combustion of fossil fuels in automobiles, trucks, and off-road engines. Ammonia (NH_3) is emitted from agricultural and industrial processes and is one of the prominent bases in most urban and rural settings. The resulting ammonium nitrate maintains a delicate balance between the particle and the gas phase HNO_3 and NH_3. Unlike the other inorganic constituents of PM (e.g., ammonium sulfate), ammonium nitrate is readily evaporated from the aerosol (as NH_3/HNO_3) at elevated temperature, and its formation is constrained by other meteorological factors like relative humidity (Seinfeld and Pandis 2016). Despite many decades of progress in emission abatement, specifically in

reducing NO_x, many urban airsheds are still plagued by ammonium nitrate (Womack et al. 2019; Li et al. 2018; Hasheminassab et al. 2014a; Gani et al. 2019), posing risk to human health (Wang et al. 2022).

Given its prominence, from a regulatory perspective it is important to understand the trends and formation mechanisms of ammonium nitrate. In part, there is an expectation that as particulate sulfate concentrations decrease, ammonium is available to neutralize nitrate, thus increasing its relative importance and formation potential in urban settings (West, Ansari, and Pandis 1999; Pye et al. 2009; Weber et al. 2016). This is purely associated with changes in particulate sulfate; if ammonium and nitrate are present in excess, the formation of ammonium nitrate can proceed readily, and will be constrained by other factors, such as available oxidants (OH, O_3, etc.), aerosol surface area, or aerosol liquid water. In Los Angeles, sulfate concentrations have decreased over the last two decades (Hasheminassab et al. 2014b), so it is expected that the importance of the AN is likely increasing relative to ammonium sulfate or bisulfate. Of course, the trend in AN formation will be limited by trends in other factors, such as available oxidants (OH, O_3, etc.), aerosol surface area, aerosol liquid water, and, importantly, its precursors NO_x and NH_3. Since AN is not directly emitted, identifying the precursor sensitivity is key for generating a control strategy, and studies have suggested that, depending on the chemical and meteorological regime, particulate nitrate can be preferentially sensitive to either NO_x or NH_3 reductions (Pusede et al. 2016; Guo et al. 2017; Guo et al. 2018; Nenes et al. 2020; Zhai et al. 2021). While NH_3 emissions have been linked to limitations in AN formation in LA (Schiferl et al. 2014), this sensitivity is likely dynamic, and it is itself a superposition of the trends in all the factors contributing to AN formation. NH_3 emissions characterized by bottom-up inventories have remained relatively constant or increased over the last two decades (see Appendix Figure S15), and top-down evidence has suggested similar trends in NH_3 globally (Warner et al. 2017; Burns et al. 2023). Since NO_x emissions and atmospheric burdens have simultaneously declined, naïve intuition says the limiting reagent for AN formation (i.e., NH_3 or NO_x is trending towards NO_x on the basis of reactant abundance.

Unfortunately, AN is one of the most difficult PM species to measure because of its temperature-sensitive thermodynamic equilibrium. It is well-documented that AN can evaporate during PM sampling (Zhang and McMurry 1992; Hering and Cass 1999). Relatively small increases in temperature or decreases in partial pressure can rapidly evaporate the ammonium nitrate from a filter, which is the EPA's federal reference method (FRM) standard for sampling PM (Appel, Tokiwa, and Haik 1981; Zhang and McMurry 1987; Zhang and McMurry 1992). During the 1990s in Los Angeles, this artifact was measured to potentially exceed 10 $\mu g\ m^{-3}$ on a single day (Hering and Cass 1999), which is essentially all of the nitrate mass, thereby introducing a significant negative bias in the total measured $PM_{2.5}$ (a regulated quantity). More recently, Chiu and Carlton, 2023, pointed out that this volatilization exists across the state of

California, appreciably influencing the FRM measurements of $PM_{2.5}$ over the last two decades. Observations reported here illustrate that AN concentrations in $PM_{2.5}$ often vastly exceed those previously reported by mass spectral methods in Los Angeles, suggesting that our previous quantification of the nitrate formation rate in Los Angeles is underestimated.

In this study, we document the persistence of AN as a ubiquitous constituent of LA aerosol, and explore the challenges to particulate nitrate measurement that have obscured the important contribution of AN to the total PM mass. Using an advancement in the design of instrumentation to enable high-time-resolution chemical analysis of the entire $PM_{2.5}$, we revisit our understanding of nitrate production and measurement in the LA Basin.

B2. Results

Persistence of ammonium nitrate PM in Los Angeles

Nitric acid (HNO_3) is the essential precursor leading to the formation of AN aerosol. HNO_3 is produced in two major ways: during the daytime when OH is present, it is formed from its reaction with NO_2; during nighttime the combination of NO_x and O_3 leads to the formation of N_2O_5 which can be hydrolyzed on aerosol to form HNO_3.

In Figure B1, we highlight both schematically. During the day, the OH-initiated oxidation of NO_2 forms nitric acid directly in the gas phase, which (in the presence of ammonia) reaches an equilibrium as ammonium nitrate in the particle phase. At night, uninhibited by the photolysis of the NO_3 radical, N_2O_5 is formed. In the presence of aerosol liquid water (Nguyen, 2015) (and sufficient surface area), N_2O_5 is hydrolyzed to form two HNO_3 in the particle phase (as opposed to the gas phase in the daytime mechanism), where it reaches its equilibrium as ammonium nitrate.

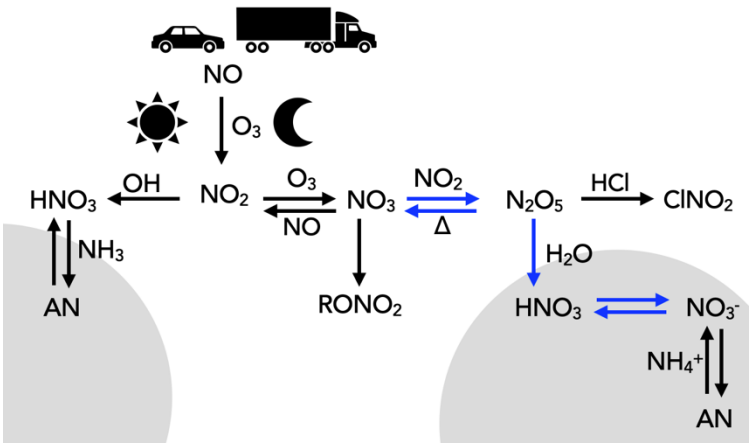

Figure B1: A schematic of the fate of NO_2 in an urban environment leading to particle phase NO_3^- formation. The left is the predominant daytime mechanism while the right is the predominant nighttime mechanism. The grey represents aerosol.

Here, we use newly available speciated and bulk measurements of $PM_{2.5}$ obtained in Pico Rivera and analysis of existing observations made in the basin in earlier campaigns (CALNEX, 2010) and by the AQMD. Details of the measurements and analysis is provided in the Appendix.

We calculate that the formation of HNO_3 and thus AN is impacted by the nighttime pathway. In urban settings with very high emissions of NO, the reaction of NO with O_3 can titrate O_3, inhibiting the formation of the NO_3 radical (Seinfeld and Pandis 2016; Brown et al. 2003). Reflecting these dynamics, decades of reductions in NO emissions in Los Angeles have led to a factor of nearly three increases in nighttime O_3 since 2000 (see Appendix Figure S22). NO_3 nighttime radical production depends on both NO_x and O_3, and so the decline in NO_x is largely compensated by the increase in nighttime O_3. During the day, decreasing NO_x concentrations should similarly cause a decrease in daytime HNO_3 production, but even here there is compensation as OH levels generally increase as NO_2 decreases. We estimate the trends in the relative formation pathways for the particulate nitrate precursors (namely gas phase nitric acid in the day and nitrate radical in the night), shown in Figure B2. The nighttime production of nitrate radical, calculated in Figure 2B(a) as the cumulative overnight nighttime production (the total amount of NO_3 produced in a single night), has in general remained nearly constant, meaning that declining NO_x concentrations compensate for increasing nighttime O_3 concentrations (see Appendix Figure S22d). We estimate that the daytime formation of HNO_3, which we calculate via a proxy for OH-exposure (see Appendix, "Trends calculations – Nitrate radical production"), has fallen by approximately half over the last 25 years, the sign of this trend consistent with observational evidence (Pollack et al. 2013). These calculations, in concert with declining sulfate concentrations over the same time span that frees NH_4^+ for interaction with NO_3^-, suggest that the

importance of the nighttime mechanism has increased relative to the daytime mechanism (Hasheminassab et al. 2014b; Weber et al. 2016).

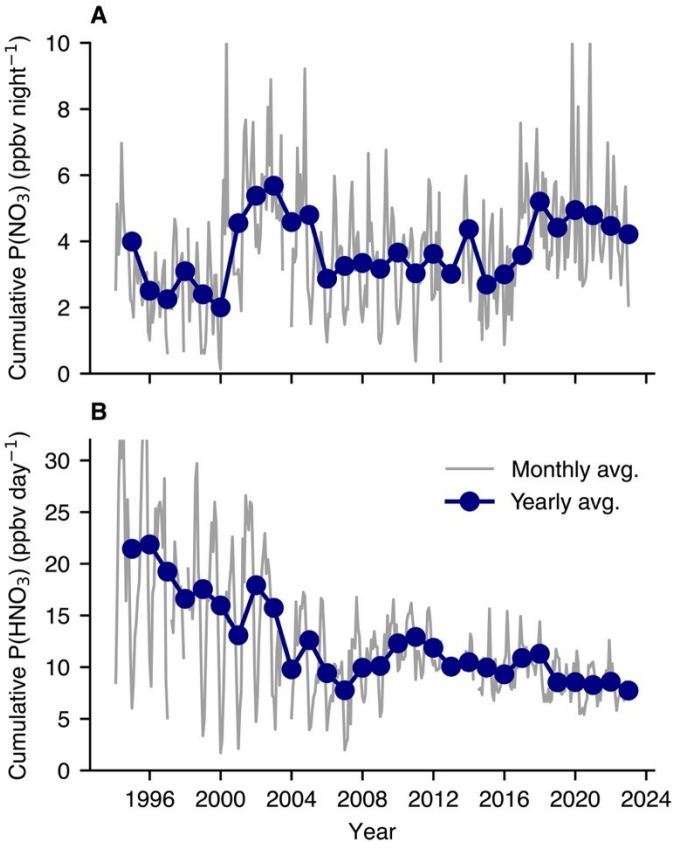

Figure B2: Decadal trends of NO_3 formation in Pasadena. (A) Estimated trend in overnight nitrate radical production. Nighttime production results only from oxidation of NO_2 by O_3, and so this rate is summed over each night to calculate cumulative NO_3 production. This represents 50% of the maximum amount of HNO_3 produced following N_2O_5 formation and hydrolysis. Loss of NO_3 via reaction with alkenes to form AN or reaction with NO or NO_3 will reduce the amount of HNO_3 formed at night. (B) Estimated trend in a proxy for the mean daytime nitric acid production in Pasadena. Daytime HNO_3 results from the oxidation of NO_2 by OH, the former of which is measured and the latter of which is parameterized by its relationship with NO.

The data presented here (Figure B5 and Appendix "Pico Rivera 2023 (Summer and Fall)") represent, to our knowledge, the first quantitative mass spectral measurements of the real-time, non-refractory $PM_{2.5}$ composition in Los Angeles. These observations are made possible with the development of the Aerodyne Aerosol Chemical Speciation Monitor (ACSM) which includes an inlet that, unlike the Aerodyne AMS (typically a PM_1 aerodynamic lens), enables quantification of the aerosol composition up to 2.5 µm in diameter (Frohlich et al. 2013; Xu et al. 2017). The ACSM used in this study was purchased for the Pico Rivera ASCENT site. Prior to its deployment, we characterized the instrument during an extended period

on the Caltech campus in Pasadena during Spring 2023. Both locations are downwind urban locations to the LA urban core, Pasadena roughly 10 miles northeast and Pico Rivera 10 miles directly east.

Appendix Figures S2 and S5 show time series measurements of the ACSM data (in addition to various other PM monitors); immediately striking are the peaks in the aerosol-phase nitrate, which always occur at night and often at magnitudes exceeding 10 μg m^{-3}. Compare these measurements to observations made in June of the 1970s (McRae, and Cass 1983), which display morning and afternoon peaks in particulate nitrate at concentrations of similar magnitude to those observed in Pico Rivera (e.g., 30 μg m^{-3} for a two-hour average). The 1970s observations feature a prominent afternoon peak that matches the timing of transport and photochemical processing along the path from downtown Los Angeles (McRae, and Cass 1983). In contrast, in 2009 and 2010, measurements from an Aerosol Mass Spectrometer (AMS) do not show this afternoon peak in particulate nitrate; instead, only an uptick in nitrate aerosol after sunset and an early morning peak is observed, consistent with a nighttime production mechanism (Hersey et al. 2011; Hayes et al. 2013). A similar trend is observed in 2022 using the AMS, though nitrate concentrations are smaller, which the authors attribute to declines in NO_x (Schulze et al. 2024). In summary, since the 1970s, the formation of particulate nitrate has shifted from a predominantly daytime process to include an important contribution from the nighttime mechanism. The amount of AN formed has declined with declining NO emissions in the basin.

It is instructive to think about the size partitioning of the AN – that is, which size fraction of the PM bears the brunt of the AN mass. The measurements analyzed by Schulze et al were made using the Aerodyne AMS (a PM_1 measurement) in both the 2009 and 2010 campaigns (PACO and CalNex) as well as in 2022 (LAAQC and CalNexT campaigns). Submicron aerosol loadings of more than 10 μg m^{-3} of particulate nitrate (hourly average) were never observed by the AMS (Hersey et al. 2013; Hayes et al. 2013; Schulze et al. 2024). In contrast, despite very similar meteorology in 2023, the $PM_{2.5}$-ACSM often measures AN in excess of 10 μg m^{-3}. We suggest that the major difference is that when AN is highly elevated, a significant fraction of the AN is found on particles greater than 1.0 μm and thus not observed by the PM_1-AMS. It would not be surprising if much of the past Los Angeles $PM_{2.5}$ was found on particles less than 1 μm, meaning that the PM_1-AMS (or other PM_1 measurement techniques) provide a reasonable estimate of the $PM_{2.5}$ mass. This has been observed with the $PM_{2.5}$ ACSM in other locations such as the wintertime San Joaquin Valley and urban Atlanta (Sun et al. 2022; Joo et al. 2021). However, mass closure with another particle sampling instrument, the Scanning Mobility Particle Sizer (SMPS), and the $PM_{2.5}$-ACSM (a PM_1 vs $PM_{2.5}$ measurement) suggests that for spring of 2023 there is a sizable amount of mass in $PM_{1–2.5}$ and that it is made up largely of ammonium nitrate (see Appendix Figures S3 and S4). Our hypothesis that there is an enhancement of secondary nitrate in larger particles is supported both theoretically (Kelvin

constraints) and observationally (Bassett and Seinfeld 1984; Liu, Prather, and Hering 2000; Hayes et al. 2013; Hughes et al. 2002). We note that the SMPS could possibly introduce drying artifacts that would bias its measurement low (Mariam et al. 2017). Furthermore, the ACSM observations are consistent with corrected filter observations of $PM_{2.5}$, adding more credence to their validity (see next section and Appendix Figure S21).

To investigate further the large particulate nitrate observations, we estimated the production of particle-phase nitrate from available precursors (namely NO_2 and O_3 at night). In brief (see Appendix for a more rigorous development), we calculate the total production of particulate nitrate over a single night from its precursors, and we compare the results with the ACSM observed growth in particulate nitrate. Essentially, we are testing this question: if transport is not important (that is, all particulate nitrate is formed locally at night), and the conversion of NO_3 radical to particle phase nitrate is 100% efficient (that is, it follows the blue arrows in Figure B1), can the gas-phase observations explain the particle phase observations? We focus primarily on the second assumption, since we believe the first approximation is reasonable given the nighttime wind speeds in LA (see Appendix CPF analysis).

These results are shown in Figure B3 for the Pasadena and Pico Rivera datasets. On at least half of the nights the particulate nitrate is, to good approximation, explained by the estimated NO_3 radical production. As shown in Figure B3, the comparison between the production of NO_3 and the increase in the amount of AN scatter around the 1:1 line - behavior we term the "local chemical production limit." In Pasadena, even when sufficient NO_2 and O_3 are present to create abundant N_2O_5, there are often nights elevated AN is not observed. These times are generally when the relative humidity is low (the white points in Figure B3(a)), consistent with inefficient hydrolysis of N_2O_5. The data points in Pico Rivera tend to show a greater diversity in results, though, when high nitrate is observed, it is almost always explained by the nighttime formation mechanism. The Pico Rivera dataset covers a much longer time period than the observations in Pasadena, and therefore a variety of meteorological and chemical conditions (e.g., production of organic nitrates or nitryl chloride, or limitations by ammonia) which may depress the formation of nitrate aerosol (Schiferl et al. 2014). We extended this analysis to other field campaigns, including CalNexT and LAAQC (see Appendix); in general, we observe that, in spring and early summer, slow hydrolysis is the primary constraint on ammonium nitrate formation (see Appendix Figure S8), while in late summer, temperature (and, therefore, partitioning of ammonia and nitric acid to the gas phase) plays an important role in limiting its formation (see Appendix Figure S9).

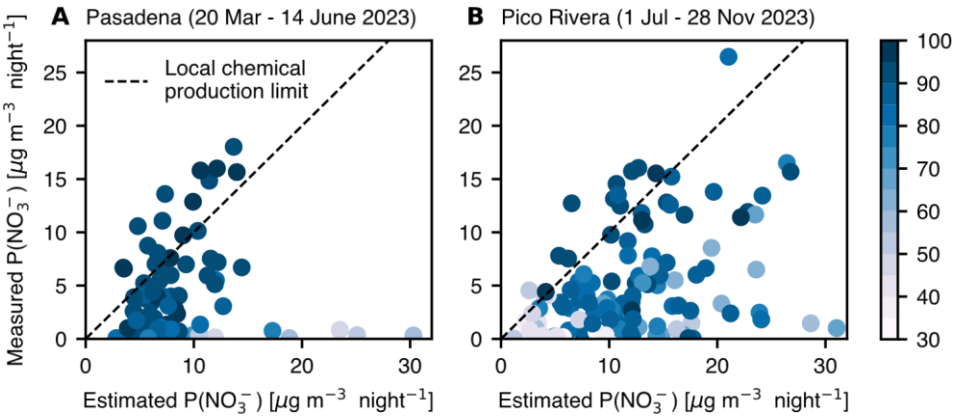

Figure B3: Estimated production of the NO_3 radical at night with measured production of NO_3^- aerosol for each day in (a) springtime Pasadena and (b) summer/fall Pico Rivera. The measurements were made by the ACSM and the overnight production estimates from precursor concentrations. Each data point represents one night in the sample period. The dashed line represents the "local chemical production limit" (that is, all NO_3 is locally converted to NO_3^-. Points are colored by the average measured nighttime RH.

Regardless of season, the nighttime formation pathway has the potential to form greater than 30 μg m^{-3} of secondary nitrate given the amount of NO_x in the LA Basin, comparable to observations in urban Beijing (Li et al. 2018; Wang et al. 2017). This analysis shows that there are ample precursors (namely NO_2, O_3, and NH_3) present to account for the ACSM observations, and that these concentrations are much higher than what has been reported over the last decade by other mass spectral measurements.

NO_x, and therefore mobile sources, remain extremely critical contributors to secondary aerosol production. The contribution of AN is often on par with or exceed that of the organic component of the aerosol, which has typically been considered to dominate secondary aerosol in LA (Nussbaumer et al. 2021; Pfannerstill et al. 2024). While controlling secondary aerosol formation is not trivial, the link between nitrate aerosol and its precursors is much better constrained than that of organic aerosol. In springtime Pasadena especially, reductions in NO_x can still serve as an effective control strategy for $PM_{2.5}$ and are on par or more important than reductions in NH_3. Depending on the meteorological and chemical regime, though, both can likely serve as controls on AN in LA, and we discuss this sensitivity further in the Appendix.

PM measurement challenges driven by ammonium nitrate volatilization

Given that ammonium nitrate remains such a critical pollutant in LA, the lack of discussion of its role is surprising. In large measure, this reflects the challenges in its quantification. A comparison of $PM_{2.5}$ measurement instruments for the 2023 Pasadena dataset is shown in Figure B4. The ACSM measures substantially more $PM_{2.5}$ than either the FRM or FEM (Teledyne T640) techniques; further, the difference can be attributed almost entirely to ammonium nitrate (i.e., larger discrepancies tend to track more

ammonium nitrate in the aerosol). Panels B4(A) and (B) illustrate that the codified EPA techniques for $PM_{2.5}$ regulation do not accurately reflect the amount of aerosol pollution in Los Angeles - significantly under-reporting the $PM_{2.5}$ mass. In contrast, the low-cost optical sensor (PurpleAir) most consistently tracks the ACSM observations (shown in B4(C)). This likely reflects preservation of AN prior to measurement by the low-cost sensor. In contrast, the FRM (Teflon filter) and the FEM (which heats the sample before optically measuring the particle scattering) are unlikely to observe AN due to evaporation.

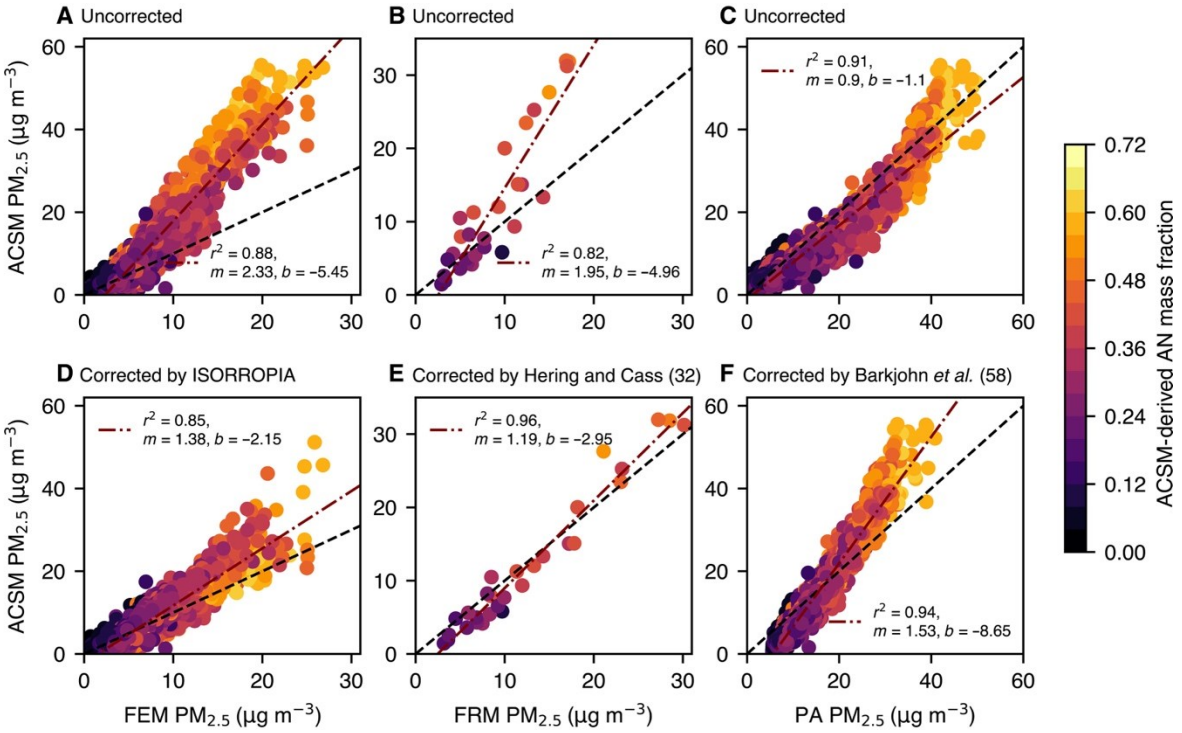

Figure B4: Comparison of PM2.5 measurements in Pasadena during the Spring of 2023. Panels (A)-(C) scatter uncorrected measurements, while panels (D)-(F) show corrections made to the data as described in the Methods. (D) adjusts the ACSM to match the FEM (i.e., decreases the ACSM-measured concentration) while (E) adjusts the FRM to match the ACSM (i.e., increases the FRM-measured concentration). The FEM and PurpleAir (PA) comparisons are hourly averages while the FRM is a daily average (measured every few days). Data points are colored by the ACSM-derived mass fraction of Ammonium Nitrate (AN). The dash-dot lines are fits to the data and the dashed lines are 1:1 lines.

While it is not possible to know the amount of ammonium nitrate measured by the FEM, FRM, or PurpleAir, we can calculate what would be expected from these sensors using the ACSM data after accounting for AN volatilization. In the case of the FRM, in 1999, an empirical parameterization was designed for these measurements and verified for PM in California (Hering and Cass 1999; Chiu and Carlton 2023), and we apply this parameterization, shown in Figure B4(E). There is a dramatic improvement in the correlation

between the ACSM and FRM (r^2 = 0.96 over the measurement period), suggesting that almost all of the bias is driven by the volatilization of ammonium nitrate. Remarkably, the Hering and Cass temperature-based parameterization (constrained by the observations of nitrate derived from the ACSM) appears to accurately capture AN loss even when much of the production is happening at night. The parameterization suggests that there is a sufficient temperature-driven volatilization over the 24 h sample period to drive a large reduction in nitrate (sometimes all of the nitrate produced).

In the case of the FEM, we use the ISORROPIA model to correct the data for loss of ammonium nitrate (see Appendix for details). This Teledyne FEM instrument heats the sample line to achieve a 35% RH for sampling, which shifts the ammonium nitrate equilibrium into the gas phase. After accounting for the evaporation of AN, the r^2 does not increase (0.88 uncorrected, 0.85 corrected), but the slope of the regression between the two instruments is much closer to 1 (2.33 uncorrected, 1.38 corrected) — again consistent with the hypothesis that volatilization of AN is responsible for most of the difference between the ACSM and FEM measurements. Evaporation of other semi-volatile species, such as many organics, could play a role in the remaining difference.

The EPA and Teledyne released a joint statement in 2024 suggesting that the FEM measurements must be adjusted to achieve better agreement between the FEM and FRM data (EPA 2024). We detail these calculations and apply them to our data in the Appendix (Teledyne-API 2024). For all $PM_{2.5}$ concentrations and temperatures, this correction leads to a reduction in the $PM_{2.5}$ determined from the Teledyne instrument. Reports suggest that across the EPA sites using these instruments both positive and negative biases relative to the FRM are found (Long et al. 2023.). In Appendix Figure S7(e) and (f) we illustrate the impact of the suggested correction. The comparison between the FEM and the FRM does not improve. Further, because this correction reduces the Teledyne measured value, the artifact introduced by ammonium nitrate volatilization is made worse. Our data illustrate the importance of having good knowledge of the aerosol speciation and size for understanding differences in measurements of PM between different methods and instruments. This effort to improve the agreement between the FEM and the FRM (and other techniques) suggests a tension between accurately reflecting the state of the atmosphere and adjusting a measurement output to match a regulatory standard (the $PM_{2.5}$ FRM). Resolving this tension will be difficult given that the legal framework for regulatory compliance rests on an analytical method that cannot accurately quantify a key component of atmospheric aerosol, AN.

In a similar vein to the FEM, many models (e.g., EPA's air quality model, CMAQ) and datasets use FRM data to benchmark model performance (Van Donkelaar et al. 2021). We compare a subset of the CMAQ EQUATES data (see Appendix for description) with FRM data collected in Pasadena, shown in Appendix Figure S16. Having established that the FRM does not capture all of the ammonium nitrate, the agreement

between the simulations and observations is spurious and suggests that the regulatory models inadequately capture the production of secondary aerosol in the LA Basin, or in other locations where ammonium nitrate is common; we discuss this further in the Appendix.

Perhaps one silver lining of this analysis is the performance of the PurpleAir sensor (Figure B4(c)); while it shows a nonlinearity, its uncorrected data best captures the range of PM magnitudes observed by the ACSM. Furthermore, corrections applied to the data set, which are themselves derived from PurpleAir/FRM comparisons (Barkjohn, Gantt, and Clements 2021), do not improve the performance of the sensor (the regressed slope goes from 0.9 to 1.53, a departure from 1), though there are a diversity of calibration types and more complex schemes which may improve its performance (Datta et al. 2020; Levy Zamora et al. 2019). It should be noted that there is a physical basis for correcting optical sensors during periods of elevated RH (due to increased light scattering by liquid water) (Barkjohn, Gantt, and Clements 2021); but this data suggests that, at least for Pasadena in spring of 2023, this correction is minor. It is important to recognize that, unlike the FRM/FEM products, the PurpleAir sensor does not heat the air and so is likely less susceptible to evaporation artifacts, particularly those due to ammonium nitrate, and so they are perhaps more suitable for deployment in regions of high ammonium nitrate pollution like Southern California, though they have their own deficiencies. Further, they are online measurements and require little supervision compared to the FRM, which is a labor-intensive technique. Higher quality optical particle counters that accurately capture the size distribution in the $PM_{1–2.5}$ size range would likely show even better agreement with the ACSM.

While we do not necessarily advocate for the replacement of FRM/FEM monitors with an ACSM or PurpleAir sensors, we do highlight the importance of speciated PM measurements. In Los Angeles, filter-based, speciated PM measurements exist at some locations, using nylon filters instead of Teflon filters to minimize evaporative losses. These measurements over the spring Pasadena measurement period, while not collocated with the ACSM, compare well (see Appendix Figure S21). To be clear, it is surprising that decades after Hering and Cass demonstrated that the use of nylon filters provided a much better method for quantifying PM, the FRM has not adopted this approach.

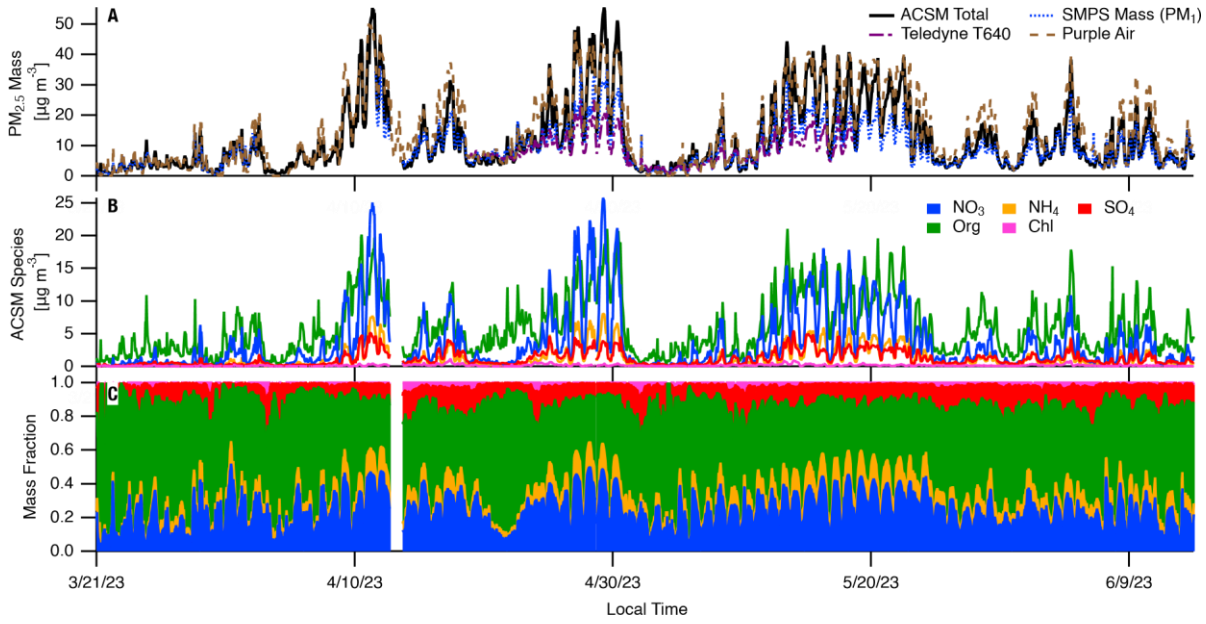

Figure B5: Pasadena Spring 2023 PM measurements. Time series of data from various instruments in Pasadena during spring and early summer of 2023. (A) shows total particle mass measurements, while (B) and (C) are speciated mass concentrations and mass fractions from the ACSM.

B3. Discussion

Aerosol in the Los Angeles basin reflects the persisting role of NO_x despite decades of reductions in its emissions. In the equinox seasons, NO_2 very effectively forms nitrate aerosol. This suggests that continued efforts to reduce NO_x emissions is essential for meeting regulatory goals. Unfortunately, over 80% of NO_x emissions in the basin (largely mobile sources), are not regulated at the local level, making efforts by the South Coast Air Quality Management District (SCAQMD) to provide an attainment plan for $PM_{2.5}$ exceptionally challenging.

It is a challenge that one of the dominant PM components in the LA atmosphere is one of the most difficult to measure. Data collected by SCAQMD demonstrate that while the Pasadena location attains the 2012 NAAQS, Downtown, Pico Rivera, and Rubidoux are in and out of compliance over the last decade (and in aggregate LA County does not attain this standard) (see Appendix Figure S18). Correcting the SCAQMD observations to account for evaporation of ammonium nitrate (only possible at the sites where an independent measurement of nitrate is made, in this case Downtown LA and Rubidoux), we find that the annual average $PM_{2.5}$ levels at these sites clearly do not meet the 2012 NAAQS, much less the strengthened 2024 requirement (see Appendix Figure S20). In a place like Los Angeles, knowledge of the PM speciation and the ability to correct for these artifacts is critical, although having correct, unbiased data in the first

place is preferable, and these observations suggest that the EPA's FRMs and FEMs are insufficient for capturing the true $PM_{2.5}$ mass. While $PM_{2.5}$ has played an integral regulatory role in reducing fine particle levels, it may be time to revisit the emphasis on $PM_{2.5}$ mass and incorporate a contemporary understanding of the complexities of the PM into our regulatory frameworks (e.g., their size distribution or speciation).

Caution is suggested in interpreting the absolute FRM PM data and its trends in regions where ammonium nitrate is high, such as in California. One natural case that arises is in the application of PM data to public health and environmental justice studies. We tested how this artifact influences our understanding of public health outcomes, with a more detailed description provided in the Appendix. Briefly, we calculated the population attributable fraction (PAF) of total (all-cause) premature attributable to long-term exposure to $PM_{2.5}$ (Burnett et al. 2018) with both uncorrected and corrected PM values in Los Angeles and Rubidoux. The results, shown in Figure B6, suggest a consistently low bias in PAF at both locations. This difference is likely an underestimate as we account for only the evaporation of ammonium nitrate, and not the potential evaporation of other semi-volatile species, such as organics (Hennigan 2016). A number of studies employ $PM_{2.5}$ data measured via FRMs to generate datasets (e.g., Van Donkelaar et al. 2021; Di et al. 2019), and in turn these data are implemented into health studies, so the health impacts associated with $PM_{2.5}$ are likely to be underestimated in those regions where ammonium nitrate is pervasive (Carter et al. 2023; Kerr et al. 2024).

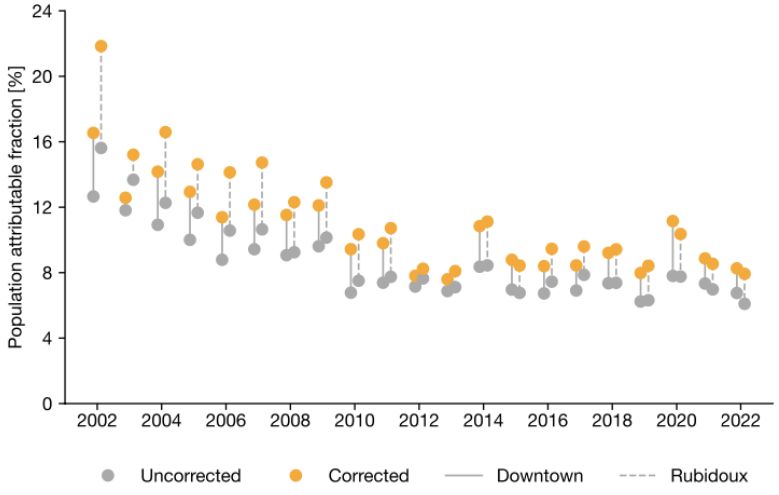

Figure B6: Time series of the population attributable fraction (multiplied by 100%) for all-cause premature mortality due to long-term (annual average) $PM_{2.5}$ exposure calculated with uncorrected concentrations and concentrations corrected for unobserved ammonium nitrate at the Downtown and Rubidoux sites.

Despite the many strides and advances in our understanding of air quality in Los Angeles, ammonium nitrate aerosol remains a top contributor to $PM_{2.5}$ mass, but a true measurement of its mass remains elusive, challenging our understanding of the atmospheric chemistry and public health implications of PM in Los Angeles.

B4. References

Acharja, P.; Ghude, S. D.; Sinha, B.; Barth, M.; Govardhan, G.; Kulkarni, R.; Sinha, V.; Kumar, R.; Ali, K.; Gultepe, I.; Petit, J.-E.; Rajeevan, M. N. Scientific Reports 2023, 13, 13667.

Agency, E. P. Update of PM2.5 Data From T640/T640X PM Mass Monitors, 2024.

Agency, U. E. P. EQUATES: EPA's Air QUAlity TimE Series Project, 2021.

API, T. Teledyne updated alignment EPA-HQ-OAR-2023-0642-0029.pdf, 2024.

Appel, B.; Tokiwa, Y.; Haik, M. Atmospheric Environment (1967) 1981, 15, 283–289.

Appel, B.; Wall, S.; Tokiwa, Y.; Haik, M. Atmospheric Environment (1967) 1980, 14, 549–554.

Ardon-Dryer, K.; Dryer, Y.; Williams, J. N.; Moghimi, N. Measurements of PM2.5 with PurpleAir under atmospheric conditions, en, 2019.

Barkjohn, K. K.; Gantt, B.; Clements, A. L. Atmospheric Measurement Techniques 2021, 14, 4617–4637.

Bassett, M. E.; Seinfeld, J. H. Atmospheric Environment (1967) 1984, 18, 1163–1170.

Brown, S. S.; Stark, H.; Ryerson, T. B.; Williams, E. J.; Nicks, D. K.; Trainer, M.; Fehsenfeld, F. C.; Ravishankara, A. R. Journal of Geophysical Research: Atmospheres 2003,108, 2002JD002917.

Burnett, R.; Chen, H.; Szyszkowicz, M.; Fann, N.; Hubbell, B.; Pope, C. A.; Apte, J. S.; Brauer, M.; Cohen, A.; Weichenthal, S.; Coggins, J.; Di, Q.; Brunekreef, B.; Frostad, J.; Lim, S. S.; Kan, H.; Walker, K. D.; Thurston, G. D.; Hayes, R. B.; Lim, C. C.; Turner, M. C.; Jerrett, M.; Krewski, D.; Gapstur, S. M.; Diver, W. R.; Ostro, B.; Goldberg, D.; Crouse, D. L.; Martin, R. V.; Peters, P.; Pinault, L.; Tjepkema, M.; Van Donkelaar, A.; Villeneuve, P. J.; Miller, A. B.; Yin, P.; Zhou, M.; Wang, L.; Janssen, N. A. H.; Marra, M.; Atkinson, R. W.; Tsang, H.; Quoc Thach, T.; Cannon, J. B.; Allen, R. T.; Hart, J. E.; Laden, F.; Cesaroni, G.; Forastiere, F.; Weinmayr, G.; Jaensch, A.; Nagel, G.; Concin, H.; Spadaro, J. V. Proceedings of the National Academy of Sciences 2018, 115, 9592–9597.

Canagaratna, M. R.; Jimenez, J. L.; Kroll, J. H.; Chen, Q.; Kessler, S. H.; Massoli, P.; Hildebrandt Ruiz, L.; Fortner, E.; Williams, L. R.; Wilson, K. R.; Surratt, J. D.; Donahue, N. M.; Jayne, J. T.; Worsnop, D. R. Atmospheric Chemistry and Physics 2015, 15, 253–272.

Carter, T. S.; Kerr, G. H.; Amini, H.; Martin, R. V.; Ovienmhada, U.; Schwartz, J.; Van Donkelaar, A.; Anenberg, S. Environmental Research Letters 2023, 18, 114008.

Chiu, Y. T. T.; Carlton, A. G. Environmental Science & Technology Air 2023, 1, 25–32.

Colonna, K. J.; Koutrakis, P.; Kinney, P. L.; Cooke, R. M.; Evans, J. S. Environmental Science & Technology 2022, 56, 6799–6812.

Crounse, J. D.; McKinney, K. A.; Kwan, A. J.; Wennberg, P. O. Analytical Chemistry 2006, 78, 6726–6732.

Datta, A.; Saha, A.; Zamora, M. L.; Buehler, C.; Hao, L.; Xiong, F.; Gentner, D. R.;vKoehler, K. Atmospheric Environment 2020, 242, 117761.

De Gouw, J. A.; Gilman, J. B.; Kim, S.-W.; Lerner, B. M.; Isaacman-VanWertz, G.; Mc-Donald, B. C.; Warneke, C.; Kuster, W. C.; Lefer, B. L.; Griffith, S. M.; Dusanter, S.; Stevens, P. S.; Stutz, J. Journal of Geophysical Research: Atmospheres 2017, 122, DOI:10.1002/2017JD027459.

Di, Q.; Amini, H.; Shi, L.; Kloog, I.; Silvern, R.; Kelly, J.; Sabath, M. B.; Choirat, C.; Koutrakis, P.; Lyapustin, A.; Wang, Y.; Mickley, L. J.; Schwartz, J. Environment International 2019, 130, 104909.

District, S. C. A. Q. M. 2022 Air Quality Management Plan, 2022.

Fehsenfeld, F. C.; Huey, L. G.; Sueper, D. T.; Norton, R. B.; Williams, E. J.; Eisele, F. L.; Mauldin, R. L.; Tanner, D. J. Journal of Geophysical Research: Atmospheres 1998, 103, 3343–3353.

Fountoukis, C.; Nenes, A. Atmos. Chem. Phys. 2007.

Fr¨ohlich, R.; Cubison, M. J.; Slowik, J. G.; Bukowiecki, N.; Pr´evˆot, A. S. H.; Baltensperger, U.; Schneider, J.; Kimmel, J. R.; Gonin, M.; Rohner, U.; Worsnop, D. R.; Jayne, J. T. Atmospheric Measurement Techniques 2013, 6, 3225–3241.

Gani, S.; Bhandari, S.; Seraj, S.; Wang, D. S.; Patel, K.; Soni, P.; Arub, Z.; Habib, G.; Hildebrandt Ruiz, L.; Apte, J. S. Atmospheric Chemistry and Physics 2019, 19, 6843–6859.

Gu, S.; Guenther, A.; Faiola, C. Environmental Science & Technology 2021, 55, 12191–12201.

Hasheminassab, S.; Daher, N.; Saffari, A.; Wang, D.; Ostro, B. D.; Sioutas, C. Atmospheric Chemistry and Physics 2014, 14, 12085–12097.

Hasheminassab, S.; Daher, N.; Ostro, B. D.; Sioutas, C. Environmental Pollution 2014, 193, 54–64.

Hayes, P. L.; Ortega, A. M.; Cubison, M. J.; Froyd, K. D.; Zhao, Y.; Cliff, S. S.; Hu, W. W.; Toohey, D. W.; Flynn, J. H.; Lefer, B. L.; Grossberg, N.; Alvarez, S.; Rappenglück, B.; Taylor, J. W.; Allan, J. D.; Holloway, J. S.; Gilman, J. B.; Kuster, W. C.; de Gouw, J. A.; Massoli, P.; Zhang, X.; Liu, J.; Weber, R. J.;

Corrigan, A. L.; Russell, L. M.; Isaacman, G.; Worton, D. R.; Kreisberg, N. M.; Goldstein, A. H.; Thalman, R.; Waxman, E. M.; Volkamer, R.; Lin, Y. H.; Surratt, J. D.; Kleindienst, T. E.; Offenberg, J. H.; Dusanter, S.; Griffith, S.; Stevens, P. S.; Brioude, J.; Angevine, W. M.; Jimenez, J. L. Journal of Geophysical Research: Atmospheres 2013, 118, 9233–9257.

Heald, C. L.; Collett, J. L.; Lee, T.; Benedict, K. B.; Schwandner, F. M.; Li, Y.; Clarisse, L.; Hurtmans, D. R.; Van Damme, M.; Clerbaux, C.; Coheur, P.-F.; Philip, S.; Martin, R. V.; Pye, H. O. T. Atmospheric Chemistry and Physics 2012, 12, 10295–10312.

Hering, S.; Cass, G. Journal of the Air & Waste Management Association 1999, 49, 725–733.

Hersey, S. P.; Craven, J. S.; Schilling, K. A.; Metcalf, A. R.; Sorooshian, A.; Chan, M. N.; Flagan, R. C.; Seinfeld, J. H. Atmospheric Chemistry and Physics 2011, 11, 7417–7443.

Hersey, S. P.; Craven, J. S.; Metcalf, A. R.; Lin, J.; Lathem, T.; Suski, K. J.; Cahill, J. F.; Duong, H. T.; Sorooshian, A.; Jonsson, H. H.; Shiraiwa, M.; Zuend, A.; Nenes, A.; Prather, K. A.; Flagan, R. C.; Seinfeld, J. H. Journal of Geophysical Research: Atmospheres 2013, 118, eprint: https://onlinelibrary.wiley.com/doi/pdf/10.1002/jgrd.50307, 3016–3036.

Hu, W.; Campuzano-Jost, P.; Day, D. A.; Nault, B. A.; Park, T.; Lee, T.; Pajunoja, A.; Virtanen, A.; Croteau, P.; Canagaratna, M. R.; Jayne, J. T.; Worsnop, D. R.; Jimenez, J. L. ACS Earth and Space Chemistry 2020, 4, 676–689.

Hughes, L. S.; Allen, J. O.; Salmon, L. G.; Mayo, P. R.; Johnson, R. J.; Cass, G. R. Environmental Science & Technology 2002, 36, 3928–3935.

Institute, H. E. Systematic Review and Meta-analysis of Selected Health Effects of Long-Term Exposure to Traffic-Related Air Pollution, 2022.

Joo, T.; Chen, Y.; Xu, W.; Croteau, P.; Canagaratna, M. R.; Gao, D.; Guo, H.; Saavedra, G.; Kim, S. S.; Sun, Y.; Weber, R.; Jayne, J.; Ng, N. L. ACS Earth and Space Chemistry 2021, 5, Publisher: American Chemical Society, 2565–2576.

Kerr, G. H.; Van Donkelaar, A.; Martin, R. V.; Brauer, M.; Bukart, K.; Wozniak, S.; Goldberg, D. L.; Anenberg, S. C. Environmental Health Perspectives 2024, 132, 037002.

Kleeman, M. J.; Cass, G. R. Environmental Science & Technology 2001, 35, 4834–4848.

Kuwata, M.; Zorn, S. R.; Martin, S. T. Environmental Science & Technology 2012, 46, 787–794.

Levy Zamora, M.; Xiong, F.; Gentner, D.; Kerkez, B.; Kohrman-Glaser, J.; Koehler, K. Environmental Science & Technology 2019, 53, 838–849.

Li, H.; Zhang, Q.; Zheng, B.; Chen, C.; Wu, N.; Guo, H.; Zhang, Y.; Zheng, Y.; Li, X.; He, K. Atmospheric Chemistry and Physics 2018, 18, 5293–5306.

Liu, D.-Y.; Prather, K. A.; Hering, S. V. Aerosol Science and Technology 2000, 33, 71–86.

Long, R. W.; Urbanski, S. P.; Lincoln, E.; Col´on, M.; Kaushik, S.; Krug, J. D.; Vanderpool, R. W.; Landis, M. S. Journal of the Air & Waste Management Association 2023, 73, 295–312.

Mariam; Joshi, M.; Khandare, P.; Koli, A.; Khan, A.; Sapra, B. Journal of Aerosol Science 2017, 111, 18 25.

McDonald, B. C.; De Gouw, J. A.; Gilman, J. B.; Jathar, S. H.; Akherati, A.; Cappa, C. D.; Jimenez, J. L.; Lee-Taylor, J.; Hayes, P. L.; McKeen, S. A.; Cui, Y. Y.; Kim, S. W.; Gentner, D. R.; Isaacman-VanWertz, G.; Goldstein, A. H.; Harley, R. A.; Frost, G. J.; Roberts, J. M.; Ryerson, T. B.; Trainer, M. Science 2018, 359, 760–764.

Middlebrook, A. M.; Bahreini, R.; Jimenez, J. L.; Canagaratna, M. R. Aerosol Science and Technology 2012, 46, 258–271.

Nault, B. A.; Campuzano-Jost, P.; Day, D. A.; Guo, H.; Jo, D. S.; Handschy, A. V.; Pagonis, D.; Schroder, J. C.; Schueneman, M. K.; Cubison, M. J.; Dibb, J. E.; Hodzic, A.; Hu, W.; Palm, B. B.; Jimenez, J. L. Atmospheric Measurement Techniques 2020, 13, 6193–6213.

Nie, W.; Wang, T.; Gao, X.; Pathak, R. K.; Wang, X.; Gao, R.; Zhang, Q.; Yang, L.; Wang, W. Atmospheric Environment 2010, 44, 4396–4403.

Nussbaumer, C. M.; Cohen, R. C. Environmental Science & Technology 2021, 55, 3549–3558.

Parrish, D. D.; Xu, J.; Croes, B.; Shao, M. Frontiers of Environmental Science & Engineering 2016, 10, 11.

Pennington, E. A.; Seltzer, K. M.; Murphy, B. N.; Qin, M.; Seinfeld, J. H.; Pye, H. O. T. Atmospheric Chemistry and Physics 2021, 21, Publisher: Copernicus GmbH, 18247–18261.

Pfannerstill, E. Y.; Arata, C.; Zhu, Q.; Schulze, B. C.; Ward, R.; Woods, R.; Harkins, C.; Schwantes, R. H.; Seinfeld, J. H.; Bucholtz, A.; Cohen, R. C.; Goldstein, A. H. Science 2024, 384, 1324–1329.

Pollack, I. B.; Ryerson, T. B.; Trainer, M.; Neuman, J. A.; Roberts, J. M.; Parrish, D. D. Journal of Geophysical Research: Atmospheres 2013, 118, 5893–5911.

Pusede, S. E.; Duffey, K. C.; Shusterman, A. A.; Saleh, A.; Laughner, J. L.; Wooldridge, P. J.; Zhang, Q.; Parworth, C. L.; Kim, H.; Capps, S. L.; Valin, L. C.; Cappa, C. D.; Fried, A.; Walega, J.; Nowak, J. B.; Weinheimer, A. J.; Hoff, R. M.; Berkoff, T. A.; Beyersdorf, A. J.; Olson, J.; Crawford, J. H.; Cohen, R. C. Atmospheric Chemistry and Physics 2016, 16, 2575–2596.

Pye, H. O. T.; Liao, H.; Wu, S.; Mickley, L. J.; Jacob, D. J.; Henze, D. K.; Seinfeld, J. H. Journal of Geophysical Research: Atmospheres 2009, 114, 2008JD010701.

Robinson, M. A.; Neuman, J. A.; Huey, L. G.; Roberts, J. M.; Brown, S. S.; Veres, P. R. Atmospheric Measurement Techniques 2022, 15, 4295–4305

Russell, A. G.; McRae, G. J.; Cass, G. R. Atmospheric Environment (1967) 1983, 17, 949–964.

El-Sayed, M. M. H.; Amenumey, D.; Hennigan, C. J. Environmental Science & Technology 2016, 50, 3626–3633.

Schiferl, L. D.; Heald, C. L.; Nowak, J. B.; Holloway, J. S.; Neuman, J. A.; Bahreini, R.; Pollack, I. B.; Ryerson, T. B.; Wiedinmyer, C.; Murphy, J. G. Journal of Geophysical Research: Atmospheres 2014, 119, 1883–1902.

Schulze, B. C.; Kenseth, C. M.; Ward, R. X.; Pennington, E. A.; Rooy, P. V.; Tasnia, A.; Barletta, B.; Meinardi, S.; Morris, M.; Jensen, A.; Huang, Y.; Parker, H. A.; Hasheminassab, S.; Day, D.; Campuzano-Jost, P.; de Gouw, J.; Jimenez, J. L.; Barsanti, K. C.; Pye, H. O. T.; Wennberg, P. O.; Seinfeld, J. H. 20245 Submitted to Environmental Science & Technology: Air.

Seinfeld, J. H.; Pandis, S. N., Atmospheric Chemistry and Physics: From Air Pollution to Climate Change; Wiley & Sons: Hoboken, N.J, 2016.

Song, S.; Gao, M.; Xu, W.; Shao, J.; Shi, G.; Wang, S.; Wang, Y.; Sun, Y.; McElroy, M. B. Atmospheric Chemistry and Physics 2018, 18, 7423–7438.

Sun, P.; Farley, R. N.; Li, L.; Srivastava, D.; Niedek, C. R.; Li, J.; Wang, N.; Cappa, C. D.; Pusede, S. E.; Yu, Z.; Croteau, P.; Zhang, Q. Environmental Pollution 2022, 292, 118254.

Thurston, G. D.; Burnett, R. T.; Turner, M. C.; Shi, Y.; Krewski, D.; Lall, R.; Ito, K. Jerrett, M.; Gapstur, S. M.; Diver, W. R.; Pope, C. A. Environmental Health Perspectives 2016, 124, 785–794.

Uria-Tellaetxe, I.; Carslaw, D. C. Environmental Modelling & Software 2014, 59, 1–9.

Van Donkelaar, A.; Hammer, M. S.; Bindle, L.; Brauer, M.; Brook, J. R.; Garay, M. J.; Hsu, N. C.; Kalashnikova, O. V.; Kahn, R. A.; Lee, C.; Levy, R. C.; Lyapustin, A.; Sayer, A. M.; Martin, R. V. Environmental Science & Technology 2021, 55, 15287–15300.

Van Rooy, P.; Tasnia, A.; Barletta, B.; Buenconsejo, R.; Crounse, J. D.; Kenseth, C. M.; Meinardi, S.; Murphy, S.; Parker, H.; Schulze, B.; Seinfeld, J. H.; Wennberg, P. O.; Blake,

D. R.; Barsanti, K. C. ACS Earth and Space Chemistry 2021, 5, 3045–3055.

Wang, Y.; Xiao, S.; Zhang, Y.; Chang, H.; Martin, R. V.; Van Donkelaar, A.; Gaskins, A.; Liu, Y.; Liu, P.; Shi, L. Environmental Science & Technology Letters 2017.

Wang, Y.; Zhang, Q. Q.; He, K.; Zhang, Q.; Chai, L. Atmospheric Chemistry and Physics 2013, 13, 2635 2652.

Wang, Y.; Xiao, S.; Zhang, Y.; Chang, H.; Martin, R. V.; Van Donkelaar, A.; Gaskins, A.; Liu, Y.; Liu, P.; Shi, L. Environment International 2022, 158, 106969.

Ward, R. X.; Baliaka, H. D.; Schulze, B. C.; Hasheminassab, S.; Crounse, J. D.; Wennberg, P. O.; Seinfeld, J. H. To Be Submitted 2024.

Weber, R. J.; Guo, H.; Russell, A. G.; Nenes, A. Nature Geoscience 2016, 9, 282–285.

West, J. J.; Ansari, A. S.; Pandis, S. N. Journal of the Air & Waste Management Association 1999, 49, 1415–1424.

Wexler, A. S.; Seinfeld, J. H. Atmospheric Environment. Part A. General Topics 1992, 26, 579–591.

Womack, C. C. et al. Geophysical Research Letters 2019, 46, 4971–4979.

Wyzga, R.; Rohr, A. Journal of the Air & Waste Management Association 2015, 65, 523–543.

Xu, W.; Croteau, P.; Williams, L.; Canagaratna, M.; Onasch, T.; Cross, E.; Zhang, X.; Robinson, W.; Worsnop, D.; Jayne, J. Aerosol Science and Technology 2017, 51, 69–83.

Zhai, S.; Jacob, D. J.; Wang, X.; Liu, Z.; Wen, T.; Shah, V.; Li, K.; Moch, J. M.; Bates, K. H.; Song, S.; Shen, L.; Zhang, Y.; Luo, G.; Yu, F.; Sun, Y.; Wang, L.; Qi, M.; Tao, J.; Gui, K.; Xu, H.; Zhang, Q.; Zhao, T.; Wang, Y.; Lee, H. C.; Choi, H.; Liao, H. Nature Geoscience 2021, 14, 389–395.

Zhang, X.; McMurry, P. Atmospheric Environment (1967) 1987, 21, 1779–1789.

Zhang, X.; McMurry, P. H. Atmospheric Environment. Part A. General Topics 1992, 26, 3305–3312.

Zhao, Y.; Tkacik, D. S.; May, A. A.; Donahue, N. M.; Robinson, A. L. Environmental Science & Technology 2022, 56, 15328–15336.

Zhu, Q.; Laughner, J. L.; Cohen, R. C. Proceedings of the National Academy of Sciences 2022, 119, e2117399119.

Recommendations

This research highlights several poorly described chemical processes that impact our understanding of trends in aerosol as NO_x emissions within the SoCAB have decreased over the past several decades. The changes in NO_x have altered the chemical pathways in the oxidation of many volatile organic compounds. This chemistry can enhance the efficiency of secondary organic aerosol formation. In addition, the reduction in NO_x emissions has resulted in changes in the pathways for formation of nitric acid which, in turn, has influenced the formation of ammonium nitrate – now often the major inorganic constituent of total PM2.5.

As nitric oxide concentrations have decreased, the lifetime of organic peroxy radicals has increased. As a result, many of these radicals – particularly those containing oxygenated functional groups – have sufficient time to undergo unimolecular hydrogen shift reactions, a process often called 'autoxidation'. The chemistry tends to result in the rapid formation of products with lower volatility resulting in higher SOA yields than currently parameterized using standard peroxy radical mechanisms. This study focused on a model system for this chemistry, glycol ethers. These compounds are used ubiquitously as solvents. We illustrate that these compounds undergo rapid H-shift peroxy radical leading to SOA formation. We find that aerosol yields increase as the rate of autoxidation increases. Importantly, this research is consistent with a parallel gas phase study performed at Caltech that demonstrated that computational chemistry can capture the temperature dependent rate coefficients of these H-shifts. Together, these studies suggest that it may be feasible to extend traditional Structure-Activity Relationship (SAR) methods to tie the gas phase chemistry to formation of aerosol. We recommend that such an approach be used to build out a SAR that will enable autoxidation to be captured in our air quality models for the wide diversity of chemicals emitted into the urban atmosphere.

The reductions in NO_x emissions have increased the amount of ozone present at night. Decades ago, NO emissions at night titrated the ozone and, as a result, limited the formation of the NO_3 radical. This is important as formation of NO_3 at night is the precursor to nitric acid which can be formed via the hydrolysis of N_2O_5. Although the fraction of NO_x being converted to nitric acid during the day has gone down, because OH levels have increased (due to the lower NO_x levels), the amount of nitric acid formed during the day has not gone down nearly as quickly. The result is that the response of nitric acid formation to the reduction in NO_x emissions has been muted. In addition, our research illustrates that the standard regulatory measurements (e.g. Method Reference ID: RFPS-1006-145) often underestimate the abundance of ammonium nitrate due to evaporated losses of ammonium nitrate as well as more volatile organic components. These findings call into question the fidelity of our past estimates of ammonium nitrate as well as the contribution of ammonium nitrate to aerosol abundance today. The research described in this

report suggests that there may be significant value in using co-located low-cost sensor PM data together with the data obtained using the standard Federal Methods to recover both the trends and current abundance of ammonium nitrate and other semivolatile organic compounds. Such data is critical for understanding how regulatory strategies can be optimized to reduce aerosol in the Los Angeles basin and, indeed, statewide.

Glossary of terms, abbreviations, and symbols.

Abbreviation	Definition
AQMD	South Coast Air Quality Management District
SoCAB	South Coast Air Basin
PM	Particulate Matter
$PM_{2.5}$	Particulate Matter with diameter less than 2.5 microns
CalNex	California Nexus, Research at the Nexus of Air Quality and Climate Change (field campaign)
SOA	secondary organic aerosol
NO_x	nitrogen oxides ($NO+NO_2$)
AN	ammonium nitrate
VOC	volatile organic compounds
OA	organic aerosol
IA	inorganic aerosol
POA	primary organic aerosol
LEV	low-emission vehicle
VCP	volatile chemical product
AMS (HR-ToF-AMS)	High-Resolution Time-of-Flight Aerosol Mass Spectrometer
LAAQC	Los Angeles Air Quality Campaign
CalNexT	California Research at the Nexus of Air Quality and Climate Change-Two field study
NR-PM_1	non-refractory particle matter with diameter less than 1 micron
PMF	positive matrix factorization
SNR	signal-to-noise ratio
GC-MS	gas chromatography mass spectrometry

WAS	whole air samples
TCCON	Total Carbon Column Observation Network
CO	carbon monoxide
BVOC	biogenic volatile organic compound
LO-OOA	less-oxidized oxygenated organic aerosol
MO-OOA	more-oxidized oxygenated organic aerosol
HOA	hydrocarbon-like organic aerosol
CIOA	cooking-influenced organic aerosol
LOA	local organic aerosol
CEPAM	California Emissions Projections Analysis Model
OH_{exp}	OH exposure
NO_y	refers to the sum of NO_x and all oxidized atmospheric odd-nitrogen species
NO_z	NO_y - NO_x
ER	emission ratio
RO_2	organic peroxy radical
HO_2	hydroperoxyl radical
IVOC	intermediate-volatility organic compounds
CMAQ	Community Multi-Scale Air Quality Model
NO_3	nitrate radical
OH	hydroxyl radical
HNO_3	nitric acid
N_2O_5	dinitrogen pentoxide
ISORROPIA-II	model that calculates the composition and phase state of an ammonia -sulfate -nitrate -chloride -sodium -calcium -potassium -magnesium -water inorganic aerosol in thermodynamic equilibrium with gas phase precursors

$P[NO_3]$	production rate of nitrate radical
FRM	Federal Reference Method
FEM	Federal Equivalence Method
BAM	beta attenuation monitoring

Appendix

Ambient measurements Pasadena 2023 (Spring and Summer)

Ambient measurements of non-refractory aerosol chemical composition were made by an Aero- dyne Aerosol Chemical Speciation Monitor (ACSM) with $PM_{2.5}$ inlet from 30 March to 14 June 2023 in Pasadena, CA from the roof of Caltech Hall (~40 m above ground level) (Frohlich et al. 2013). This contrasts previous aerosol mass spectral measurements in Pasadena, e.g. (Hayes et al. 2013; Schulze et al. 2024), that reported the non-refractory PM_1 with an Aerodyne HR-ToF-AMS. Aerosol was sampled through 7 m of 3/8" stainless steel line attached to a Teflon-coated cyclone mounted to the roof of Caltech Hall. The cut size was set to 3.5 µm (recall this ACSM is a $PM_{2.5}$ measurement, and a typical 2.5 µm cut would serve to doubly-cut the aerosol). The sample is dried by a Nafion dryer to an RH below 15%. Data were analyzed in Tofware are the composition dependent collection efficiency (CDCE) is applied (Middlebrook et al. 2012).

Throughout the campaign, ammonium is roughly balanced by the measured anions (sulfate, nitrate, and chloride), see Figure Appendix Figure S1, suggesting little nitrate in the form of organic nitrates.

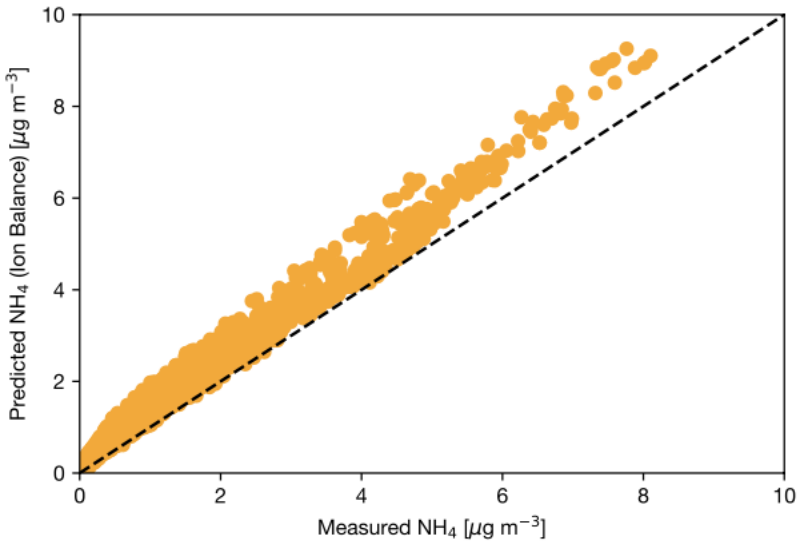

Appendix Figure S1: Ion balance for the measurements in springtime Pasadena 2023. Predicted NH^{+4} is calculated from the sum Cl^- + NO_3^-+ $2SO_4^{2-}$. Each data point is an hourly average and the dotted line represents 1:1.

The PM_1 volume distribution was measured by a Scanning Mobility Particle Sizer (TSI, Classifer Model 3082, water CPC Model 3789). The SMPS mass is inferred from the volume through estimation of the aerosol density (Hu et al. 2020):

$$\rho_{aer} = (SO_4 + NH_4 + NO_3 + Chl)/1.75 + Org/\rho_{aer} \quad (1)$$

where SO_4, NO_3, NH_4, Chl, and Org are the measured concentrations of the ACSM, 1.75 is the conversion for the density of inorganic constituents, and ρ_{org} is the density of the organic aerosol inferred from the O:C and H:C ratios (Canagaratna et al. 2015; Kuwata, Zorn, and Martin 2012). We note that Hu and colleagues further correct the aerosol organic density above 1.6 g cm^{-3}, which may bias our SMPS-inferred mass a bit high in this study, though this difference in the organic density is often less than 1% that post-correction, which represents an even smaller difference to the total aerosol difference (Hu et al. 2020).

$PM_{2.5}$ is also measured at Caltech Hall using a Teledyne T640 monitor, a Federal Equivalence Method (FEM). This measurement is optical, using Lorenz-Mie theory to convert scattered light into particle loading. The sample line is dried to a 35% RH by heating the incoming sample, and these temperatures reported by the instrument. Measurements of $PM_{2.5}$ are also made by a PurpleAir PA-II monitor. This too is an optical measurement, interring mass concentration from scattered light Ardon-Dryer et al. 2019. Data were accessed through PurpleAir's API. The standard PurpleAir Plantower ATM algorithm output (for outdoor data) are used.

Additional trace gas and meteorological data are provided by an SCAQMD monitoring station in Pasadena on Caltech's campus, roughly 500 m away from Caltech Hall. These data include: wind speed, wind direction, relative humidity, temperature, CO, NO, NO_2, O_3, and $PM_{2.5}$ (FRM). Data were accessed through the Air Quality and Meteorological Information System (AQMIS).

Pico Rivera 2023 (Summer and Fall)

Similar measurements to Pasadena were made in Pico Rivera, about 10 miles south of Pasadena. While it is comparable to Pasadena in its proximity to a downwind urban plume from downtown Los Angeles, it contrasts Pasadena in its proximity to industrial activities and its distance from the foothills of the San Gabriel Mountains (adding meteorological differences). This site is part of the ASCENT project (Atmospheric Science and Chemistry mEasurement NeTwork).

Ambient air was sampled through a cyclone to the ACSM and SMPS via 1/4" stainless steel tubing through a cyclone at a total flow rate of 2 lpm (0.1 lpm for the ACSM, 0.6 lpm to the SMPS, and 1.3 lpm make-up

flow). We note the cyclone cutoff diameter is 3.5 µm, as described in the previous section. Calibration and data analysis procedures are the same as previously provided.

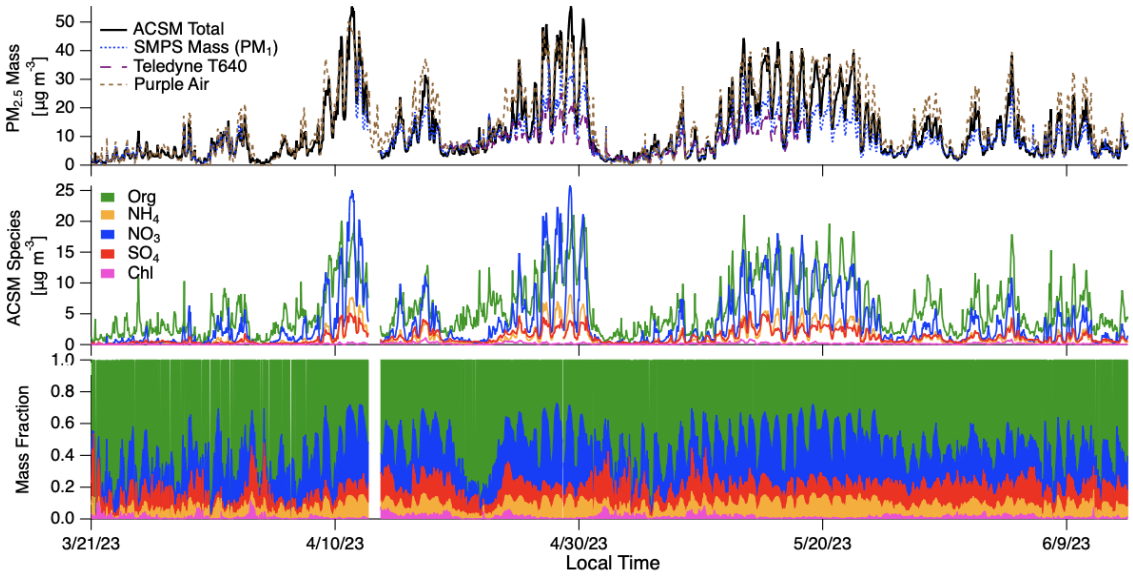

Appendix Figure S2: Time series of data from various instruments in Pasadena during spring 2023.

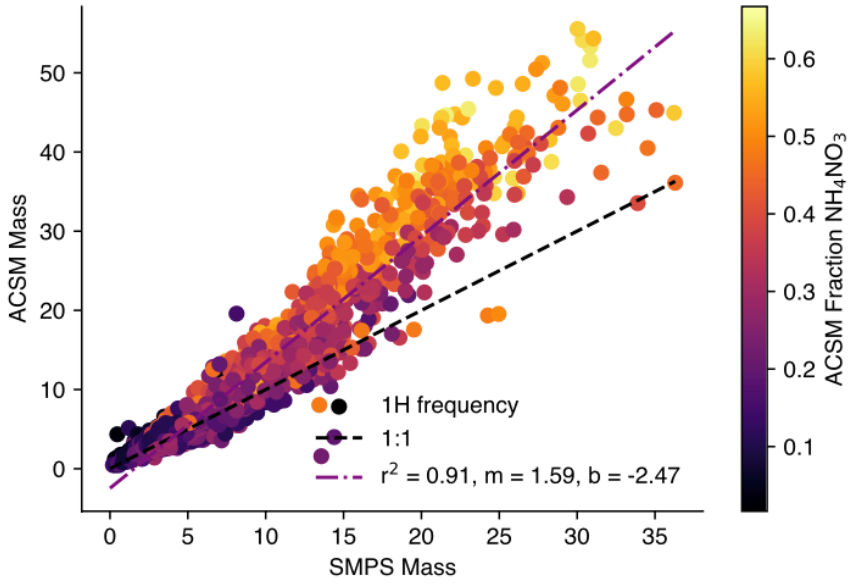

Appendix Figure S3: Scatter plot of time series measurements made by the ACSM and the SMPS. SMPS mass is inferred from the aerosol density calculated in Equation 1.

Again, SCAQMD provides the following QA/QC measurements: FRM $PM_{2.5}$, O_3, NO_X, and meteorological data (temperature, relative humidity, and wind speed/direction). Additional particle-phase measurements include: an aethalometer (AE33, Magee), a metals monitor (SCI Xact 625i), and the SMPS. Additionally, PurpleAir PA-II sensors are deployed at the site.

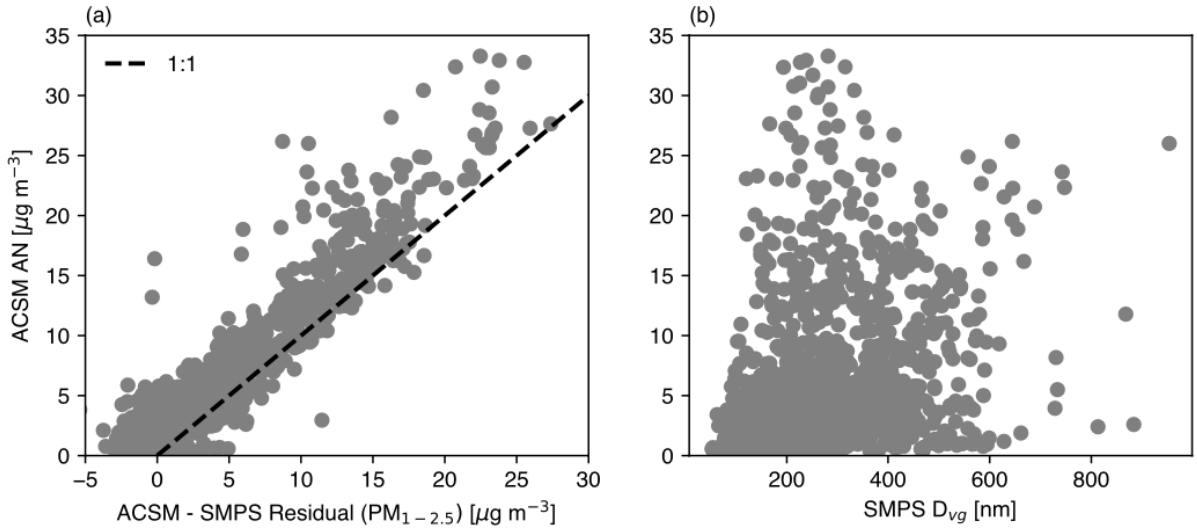

Appendix Figure S4: (a) Scatter of the measured ACSM ammonium nitrate (AN) against the residual between the ACSM mass and the inferred SMPS mass, which is essentially the mass $PM_{1–2.5}$. The close correlation suggests much of this mass is ammonium nitrate. (b) Scatter plot of the diameter of average volume measured by the SMPS and the ACSM ammonium nitrate.

Pasadena 2021 (Summer)

In the summer of 2021, ambient measurements were made as part of the RECAP campaign in Pasadena by multiple stakeholders, including Caltech, NOAA, EPA, UC Davis, and others. In particular, we are interested in two CIMS measurements, one made by Caltech and one by NOAA. Briefly, these two measurements use differing reagent ions, CF_3O^- in the case of Caltech and I^- in the case of NOAA (Crounse et al. 2006; Robinson et al. 2022). Both instruments measure HNO_3, a notoriously difficult species to measure for a variety of reasons; in particular, here, we focus on particle phase interferences, which have been known historically to affect HNO_3 measurements from filter techniques, though, to our knowledge, not yet published for CIMS techniques from these specific instruments (Appel et al. 1980; Fehsenfeld et al. 1998).

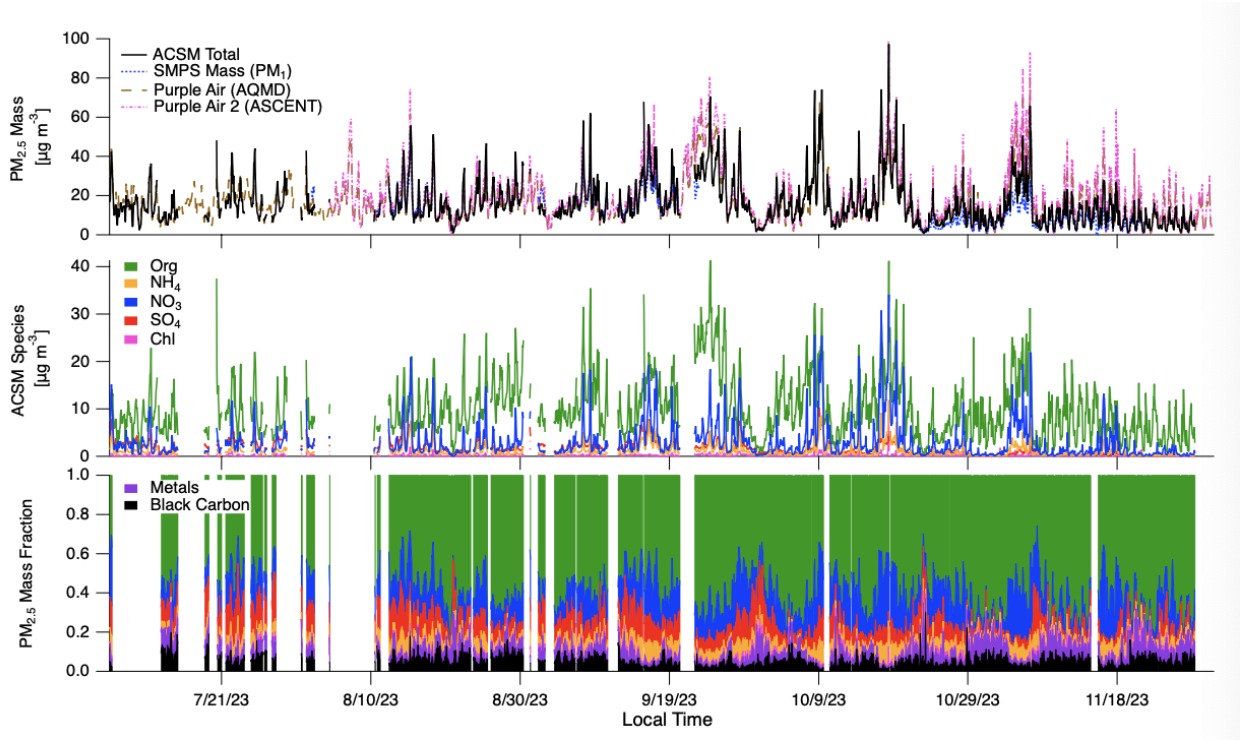

Appendix Figure S5: Time series of data from various instruments in Pico Rivera during summer and fall of 2023.

During the campaign, the Caltech and NOAA measurements report significantly different measurements of HNO_3, shown in Figure B5 (Main Text – Part B). The comparison of these measurements is shown in Appendix Figure S6.

While speciated $PM_{2.5}$ was not measured, we do have speciated PM measurements from the HR-ToF-AMS, and we can infer the $PM_{2.5}$ composition as follows: (1) we take the total mass of $PM_{2.5}$ from the PurpleAir sensor at the ground site and (2) we infer the composition of the $PM_{1-2.5}$ as either uniform to the PM_1 or entirely enriched in ammonium nitrate. To the first point, we believe the total mass of $PM_{2.5}$ is (to good approximation) represented by the PurpleAir sensor, as pointed out in the main text. To the second point, we also believe that both of these cases are possible given previous literature (e.g., Bassett and Seinfeld 1984) and our results in the Main Text. So, the uniform $PM_{1-2.5}$ composition with the PM_1 represents likely a lower bound on the amount of ammonium nitrate present in the $PM_{2.5}$, and the enriched case represents the upper bound.

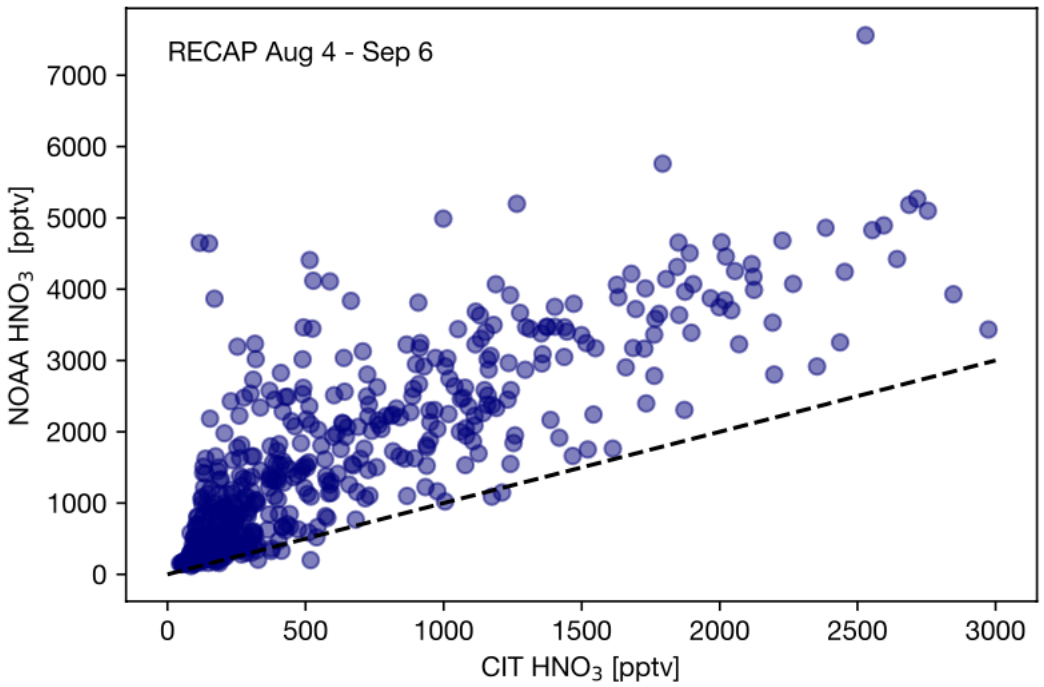

Appendix Figure S6: Scatter plot of HNO_3 measurements made by CIMS from the Caltech (CIT) and NOAA, resampled to an hourly timescale. The dotted line represents 1:1. The excess HNO3 measured by NOAA is attributed to evaporation of ammonium nitrate in the long heated inlet.

Figure B5 (Main Text – Part B) demonstrates that, if evaporated particulate nitrate drives the differences in the two CIMS measurements, there is likely sufficient particulate nitrate present on any given day to explain the difference. Furthermore, the timing of the differences (e.g., largest differences at night) is consistent with the nighttime formation mechanism for ammonium nitrate.

Pasadena 2022 (Summer)

In the summer of 2022, a series of AMS and CIMS measurements were made in the spring and summer of 2022 in Pasadena, CA, termed LAAQC (15 May — 23 June) and CalNexT (2 July — 14 August) at Caltech Hall, the same location as for our ACSM measurements. We refer the readers to the methods and Supplement of Schulze et al. for specific information on the measurements (Schulze et al. 2024).

To calculate the speciated $PM_{2.5}$, we follow the same protocol as in the 2021 AMS dataset, employing the PurpleAir to get the magnitude of the total mass of the $PM_{2.5}$ and using the AMS and assumptions about the $PM_{1-2.5}$ to tease out the amount of secondary nitrate.

Instrument corrections Federal Reference Method

To correct the Federal Reference Method data at various SCAQMD sites, we used a parameterization proposed by Hering and Cass, adapted recently by Chiu and Carlton, herein briefly described (Hering and Cass 1999; Chiu and Carlton 2023). Three mechanisms for inducing loss are considered: (1) the depletion of ammonia and nitric acid ahead of the filter, (2) an increase in temperature of the filter above ambient, and (3) pressure drop across the filter. Using the dissociation constant for ammonium nitrate (K_{amb}), the loss is calculated as:

$$\Delta NO_3^- = \frac{745.7}{T_R}\frac{1}{24}\sum_{i=1}^{24}\sqrt{K_{amb}} \quad (2)$$

where ΔNO_3^- is the loss of nitrate in [$\mu g\ m^{-3}$], T_R is a reference temperature, and 745.7 results from unit conversions. For details of the calculation of the dissociation constant and other relevant thermodynamic quantities (such as the deliquescence relative humidity), we refer the reader to the above citations.

Important to note, this calculation represents an asymptotic loss rate of nitrate, while the real situation is time-dependent. In other words, the depletion of nitric acid or ammonia above the headspace of the filter, in addition to the temperature of the filter, are time-variant quantities, so the evaporation rate of ammonium nitrate (or condensation, if applicable) is a function of time. Here, the loss rate is bounded by true measurements of the particulate nitrate; in the work of Hering & Cass a denuded nylon filter is used to know the true value, and in this work, we employ both the nylon filter and the ACSM to bound the measurements. With known amounts of nitrate, we ensure an upper limit to the volatilization of nitrate.

Federal Equivalence Method

To correct the data for the Federal Equivalence Method, in this case the Teledyne T640 data, it is useful first to understand its operating principles. In brief, to make its measurement optically, and to ensure comparability of the aerosol population in various humidities, the instrument heats the sample to achieve a relative humidity of 35% (compare this to the ACSM which uses a Nafion dryer, which can ostensibly introduce artifacts as well (El-Sayed, Amenumey, and Hennigan 2016). This heating could drive volatilization of the semi-volatile species in the sample; we employed the thermodynamic model ISORROPIA-II to correct for this artifact (Fountoukis and Nenes 2007).

Briefly, ISORROPIA-II is a thermodynamic equilibrium model which solves for the equilibrium state of various species, including ammonium, nitrate, and sulfate. There are two modes of operation: forward and reverse. In the forward mode, the equilibrium state is calculated for known gas and aerosol phase species

plus temperature and relative humidity. In the reverse mode, only particle phase concentrations are known, and the model outputs the gas, liquid, and solid phases. This is often useful in interpreting ambient observations, where often only particle phase values are known. We also note errors in the ISORROPIA-II reverse mode, principally with respect to pH (Song et al. 2018), though we do not expect this pathology to impact the results here.

To start, we run the model in reverse mode for the following conditions: the ACSM-measured sulfate, nitrate, ammonium, chloride, and the temperature and relative humidity measured at the TCCON station on Caltech's campus (roughly 100 m away). Phase state was set to metastable and crustal species were ignored. With this information, the aerosol and gas phase species concentrations were estimated.

The Teledyne instrument records the temperature and relative humidity of the sample in real-time; we use these measurements to correct for the temperature-driven volatilization of ammonium nitrate under the assumption that the sample arrives at thermodynamic equilibrium. This is not a terrible assumption, as we know the ammonium nitrate system can reach thermodynamic equilibrium on the order of minutes depending on the distributions of size and phase state (Wexler and Seinfeld 1992). Using the results of the reverse run of ISORROPIA as a starting point, we run the model in forward mode using the total calculated aerosol and gas nitrate, sulfate, ammonium, and chloride; however, we use the sample temperature and relative humidity reported by the instrument. In essence, our goal is to re-partition these inorganic constituents between the aerosol and gas phases at the elevated temperature reported by the instrument. From here, we extracted the expected aerosol-phase concentrations of the nitrate, sulfate, and ammonium, and we adjusted the ACSM concentrations to match these values, thereby allowing the ACSM measurement to reflect any temperature-driven volatilization in that the Teledyne instrument would experience. The results of the correction are displayed in the Main Text (Figure B4(A) and (D)) and reproduced in Appendix Figure S7 (a) and (b).

Sensitivity studies were performed to test the efficacy of the reverse mode of ISORROPIA- II. We inflated the gas phase concentrations of nitrate (HNO_3) and ammonia by 2 and 10x the output of the initial reverse mode simulations to test how sensitive the re-partitioning is to the gas phase concentrations (which are unmeasured). For a greater gas-phase concentration of either species, we would expect the particle-phase to retain more of the species, thereby limiting the artifact induced by heating of ammonium nitrate. These tests are shown in Appendix Figure S7 (c) and (d). We observe in either case that even if the reverse mode of ISORROPIA-II initially output gas concentrations that are too low, by inflating that gas-phase concentration we can still create good agreement just by repartitioning ammonium nitrate. Primarily, we are interested in the plausibility of ammonium nitrate partitioning in explaining the differences between the ACSM and Teledyne instruments, and while quantitatively this correction is quite accurate, we

acknowledge that this technique is mechanistically qualitative, as we never actually constrain the amount of ammonium nitrate in this instrument.

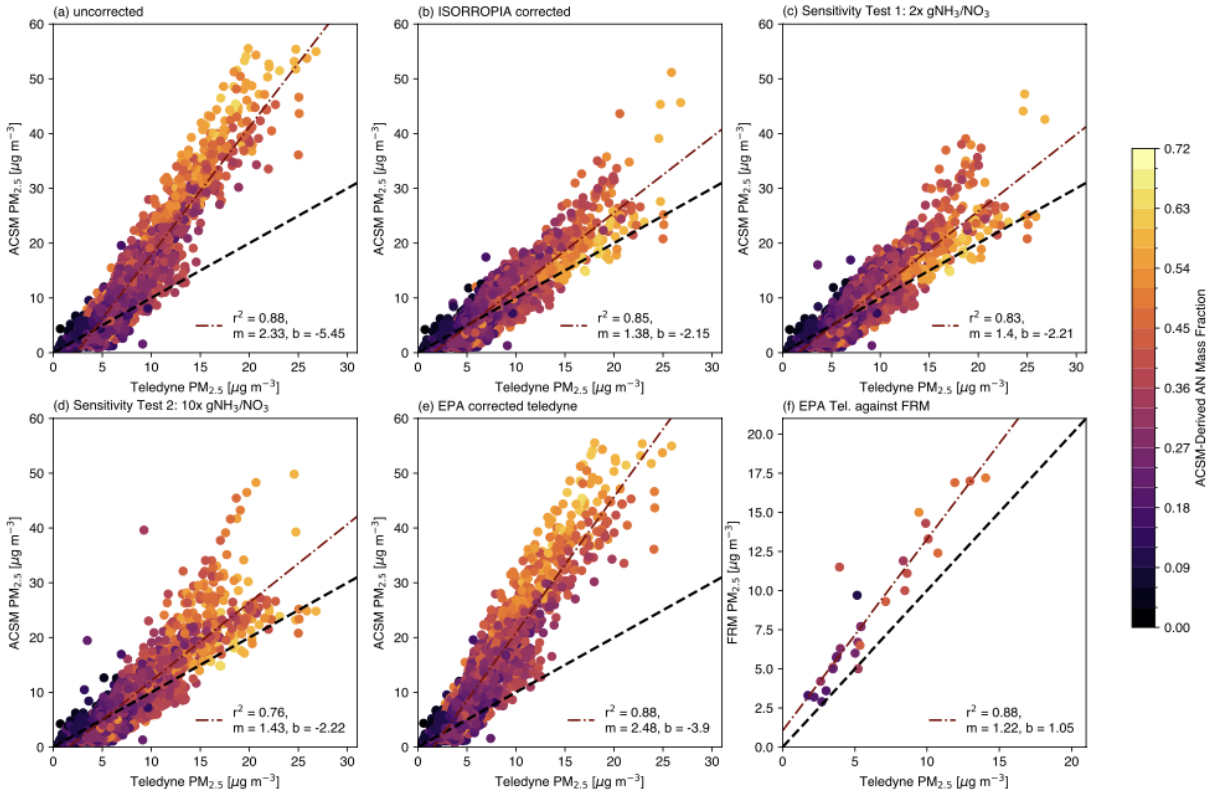

Appendix Figure S7: Comparison of various $PM_{2.5}$ measurements in Pasadena during the Spring of 2023 to the Teledyne (FEM). (a)-(b) are reproduced from the Main Text. (c)-(d) are the sensitivity studies for the ISORROPIA corrections. (e)-(f) adjust the Teledyne by the EPA/Teledyne correction equations released in May of 2024.

EPA Corrections to the Teledyne T640/X (FEM)

In May of 2024, the US EPA issued guidance under 40 CFR 53.14 to retroactively adjust the data output by Teledyne T640/X monitors; all future data published using this FEM would be amended with this modification Agency 2024. The purpose of this correction is to improve a consistent positive bias observed between the T640/T640X instruments and the Federal Reference Method. The report from Teledyne further details the positive bias to be larger at cooler temperatures. In general, this calibration applies a temperature correction to the Teledyne data as follows:

$$PM_{corr} = \{ 0 \ .813233 \times PM_{meas} T < 20, PM_{meas} \leq 10 PM_{meas} - 1.861 T < 20, PM_{meas} > 10 0.813233 \times PM_{m}$$

where PM_{meas} is the output concentration by the T640/X [μg m^{-3}], T is the temperature [˚C], and PM_{corr} is the corrected $PM_{2.5}$ value to report [μg m^{-3}]. Uniformly, this data correction corrects down the Teledyne data concentration, which is opposite of the biases reported in this work. The results of the correction applied to the 2023 Pasadena dataset are shown in Appendix Figure S7 (e) and (f), where we compared the adjusted values to the ACSM and the FRM. In both cases, the Teledyne underestimates the reported concentration, further generating a negative bias of the instrument performance, as expected based on the operating principles of the instrument and the thermodynamics of the aerosol population.

Trends calculations Nitrate Radical Production

In general, the production of nitrate radical is governed by one reaction:

$$O3(g) + NO2(g) -> NO3(g) + O2(g) \qquad k = 1.2 \times 10^{-13} \exp\left(-\frac{2450}{T}\right). \qquad (3)$$

This is the only source of nitrate radicals in the nighttime urban atmosphere, where it is the dominant radical initiating chemistry. During the day, NO_3 is photolyzed, so its chemistry is not considered (though aerosol-phase nitrate can be produced via OH-initiated oxidation of NO_2).

$$P(NO3) = k(T)[NO2][O3] \qquad (4)$$

We estimate the production rate of nitrate radicals via the relationship which gives the instantaneous production rate based on measured NO_2 and O_3 concentrations and the temperature. We sum this production rate over the evening (determined by the measured solar irradiance at Caltech's TCCON station) to estimate the total production of NO_3 radicals. Ultimately, the conversion of NO_3 radicals to aerosol phase NO_3^- is governed by the efficiency of the following reactions:

$$NO3(g) + NO2(g) -> N2O5(g) \quad (5)$$

$$N2O5(g) + M -> [\Delta]NO3(g) + NO2(g) + M \quad (6)$$

$$N2O5(g) + H2O(aq) -> 2HNO3(aq) \quad (7)$$

$$HNO3(aq) + H2O(aq) -> NO3-(aq) + H3O+(aq) \quad (8)$$

$$NO3-(aq) + NH4+(aq) -> NH4NO3(aq). \quad (9)$$

If we assume (1) the conversion of nitrate radical to particle-phase nitrate was local (i.e., it is sufficiently rapid that the appearance of the particle phase nitrate corresponding to changes in NO_2 and O_3 can be observed at the same location), and (2) that the particle-phase nitrate is in turn not transported away, then we can estimate the production of particle-phase nitrate solely from NO_2 and O_3. In essence, we want to know how efficiently every molecule of NO_2, if following the reactions (3) and (5)-(9), is converted to particle phase NO_3^-.

These calculations are depicted in the Main Text in Figure B2 and reproduced and amended with further data in Appendix Figures S8 and S9. From trace gas measurements, we sum the cumulative nighttime production of nitrate radical from NO_2 and convert this into particle-phase nitrate through the above chemical reactions, Then, we compare this to the observed amount of nitrate formed overnight measured by the ACSM or AMS, the latter of which has been adjusted to reflect $PM_{2.5}$ as previously described. For each night, a measurement that falls close to the 1:1 line (which we have called the "local chemical production limit") suggests that the NO_2 is efficiently converted to particle-phase nitrate in the absence of transport.

For springtime and early summer, we see much of the data clusters at the local chemical production limit, which suggests that reductions in NO_x may serve as an effective control strategy for particulate nitrate, which has been suggested in other locations and seasons (Pusede et al. 2016; Acharja et al. 2023). Across this time period we see that the primary constraint on particle- phase nitrate formation is water, suggesting a limited hydrolysis of N_2O_5. In contrast, in the summer (Pico Rivera and CalNexT) we see fewer days which tend towards this local chemical production limit, which potentially suggests limitations through other mechanisms, for instance NH_3, or simply temperature, shown by Appendix Figure S8. Indeed, a variety of chemical and physical constraints to ammonium nitrate formation have been documented, so its control can not only be left up to NO_x mitigation strategies (Wang et al. 2013; Womack et al. 2019).

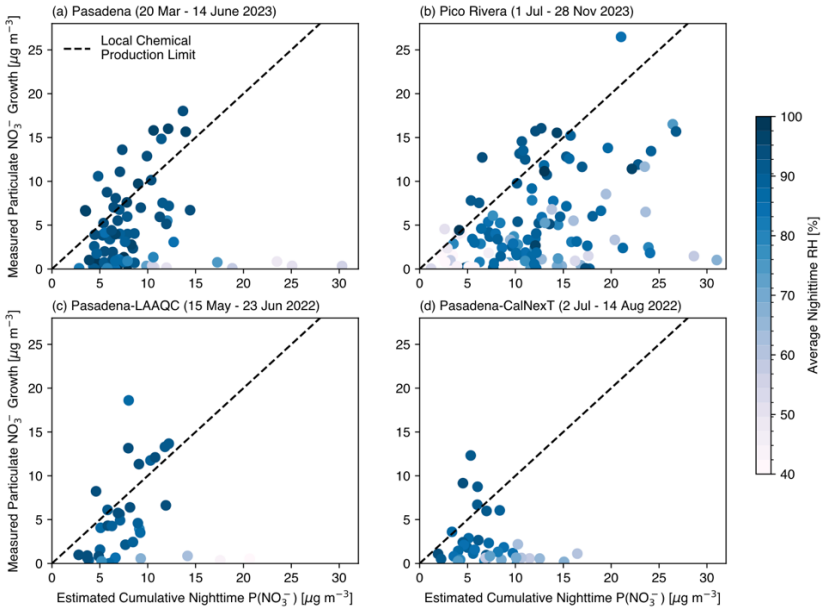

Appendix Figure S8: Estimated and measured production of NO_3^- aerosol for each day in (a) 2023 spring-time Pasadena, (b) 2023 summer/fall Pico Rivera (c) 2022 spring/early summer Pasadena, (d) 2022 late summer Pasadena. Data points represent a single night and are colored by mean RH over the night.

To estimate the amount of HNO_3 produced during daytime, knowledge of the OH exposure is needed. Here we follow the approach described by Van Rooy et al., 2021 and reported in Schulze, 2025. Airmass OH exposure is calculated using the ratio of VOC reactivities with OH, and represents the airmass OH exposure at approximately midday (Parrish et al., 2007; de Gouw et al., 2017). VOC measurements were made across multiple campaigns (e.g., Van Rooy et al., 2021), and these measurements corrected for background CO. The array of OH exposures presented in this work spans about a decade of data (i.e., CalNex in 2010 and LAAQC/CalNexT in 2022), and have been compiled elsewhere (Schulze et al., 2024). Other work derived from remote sensing measurements has also suggested an increase in OH in the basin (Zhu, Laughner, and Cohen 2022) over similar timescales. With the OH_{exp}, we can then infer a proxy for nitric acid production, which we take to be the product: $P(NHO_3) = OH_{exp}[NO_2]$.

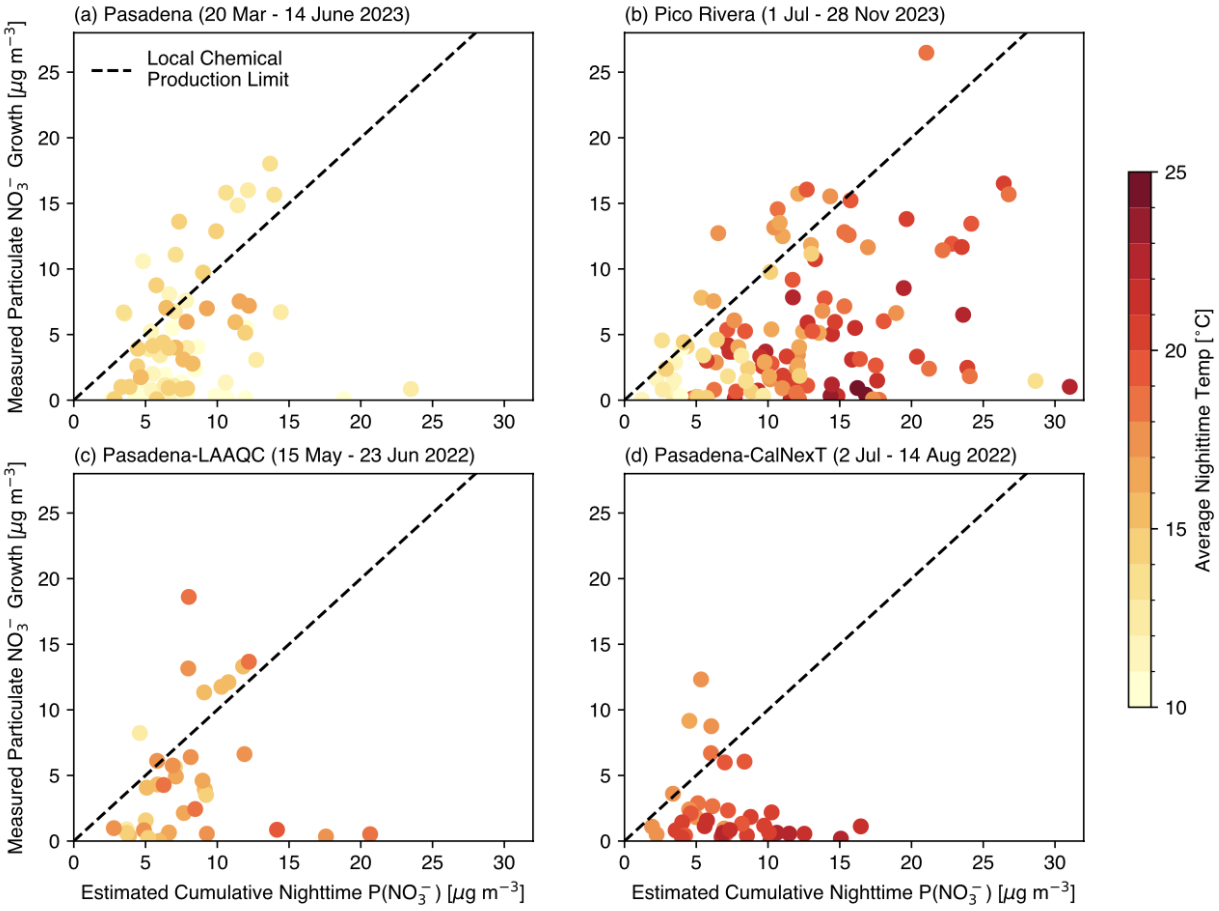

Appendix Figure S9: Estimated and measured production of NO_3^- aerosol for each day in (a) 2023 spring-time Pasadena, (b) 2023 summer/fall Pico Rivera (c) 2022 spring/early summer Pasadena, (d) 2022 late summer Pasadena. Data points represent a single night and are colored by mean temperature over the night.

Implicitly, this trend will suggest a competition between declines in NO_x in the basin and increases in OH. With a knowledge of the decadal changes in the production of nitric acid and nitrate radical, which are the presumed dominant contributors to daytime and nighttime nitrate aerosol respectively, then we can, at a high level, understand changes in the relative importance of day and nighttime formation processes in nitrate aerosol.

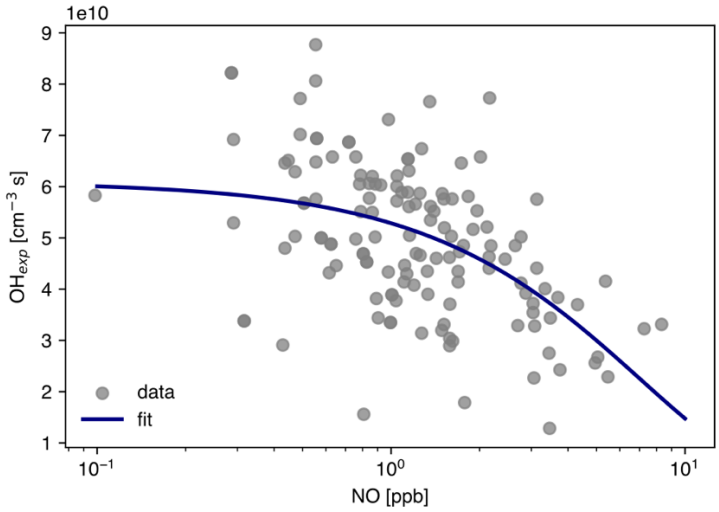

Appendix Figure S10: Fit estimation for OH exposure. Data from Schulze et al. (Schulze et al., 2024).

Thermodynamics of Nitrate Partitioning

Reductions in either (or both) NO_x and NH_3 can act as levers for reducing the atmospheric burden of AN. So, it is useful to identify which of these (if either) is the limiting reagent, so it can be targeted for control. For the LA basin in 2010, it has been suggested that the AN is sensitive both to total NH_3 and total NO_3 burdens, meaning that reducing emission of either of these precursor species can serve as an effective strategy for reducing the aerosol burden (Nenes et al. 2020). The two limitations (by NO_x or by NH_3) are summarized well by Guo and coauthors (Guo et al. 2018). Briefly:

1. *NO_x Control.* Reduction in the precursor of HNO_3 formation, namely NO_x, should reduce the burden of AN aerosol by removing nitrate from the system. This is only effective if a majority of the total NO_3 is partitioned to the particle phase, which happens under conditions of less acidic aerosol and higher aerosol liquid water content.

2. *NH_3 Control.* Reduction in NH_3 concentrations primarily impacts particle pH, increasing the acidity. This shifts the partitioning equilibrium of the nitrate out of the aerosol-phase and into the gas-phase, thereby reducing AN. If particle pH is sufficiently high and all sulfate neutralized, reductions in NH_3 may not substantially impact the particle-phase concentration of nitrate, as it will likely already reside in the aerosol phase.

Since 2010 in Los Angeles, NO_x concentrations and emissions have declined while NH_3 emissions have remained largely stagnant. The trend in NH_3 concentrations is less well-constrained; measurements in late spring/early summer of 2010 in Pasadena suggest an average daily NH_3 concentration of 2 $\mu g\ m^{-3}$, whereas measurements in late summer of 2021 suggest somewhere around 5 $\mu g\ m^{-3}$. Because of the meteorological and seasonal impacts on emissions and atmospheric concentrations, it is impossible to say whether the ambient concentration is increasing based on those two data points; however, it is likely not decreasing, a trend consistent with measurements in many parts of the world (Warner et al. 2017; Burns, Chandler, Dunham and Carlton 2023). So, with declines in NO_x and not NH_3 it stands to reason that ammonium nitrate formation may be trending towards a NO_x limitation judged on atmospheric abundance alone. This of course misses the complicated interplay between pH (modulated by aerosol sulfate), aerosol liquid water, temperature, and other factors.

To examine these limitations more rigorously, we assessed the partitioning of nitrate for measurements made during the RECAP campaign (Pasadena Summer 2021). While the composition of the $PM_{2.5}$ was not measured, as discussed, we try to infer the dynamics of the nitrate partitioning to generalize about the trends in nitrate production over the last decade. To determine the partitioning, ISORROPPIA-II was run in forward mode using the following inputs: the $PM_{2.5}$ speciated mass is assumed to be that of the enriched case, the HNO_3 concentration is taken from the CIT CIMS, and the NH_3 concentration is taken from the Picarro measurements. Crustal species are ignored. To test limitation by either NO_x and NH_3, we run five simulations variations: a base case (all concentrations as measured), two where the total NH_3 and total NO_3 (gas and particle phase sum) are independently reduced by 50%, and two where they are reduced by 90%

The results of these simulations are shown in Appendix Figure S12. Akin to the finding of Guo and colleagues (Guo et al. 2018) in the Netherlands, we find that for the summer of 2021, LA exhibits a stronger initial sensitivity to reductions in total NO_3, suggesting that controls on NO_x remain an important control strategy for PM. For a large reduction in total NH_3, there is a strong enough shift in the pH to influence the nitrate partitioning (away from the particle-phase), though the reduction in PM is likely more modest at lower total NH_3 reductions. Furthermore, following Nenes et al. 2020, we identified that for much of the campaign, predicted aerosol pH and aerosol liquid water content suggest that the air masses are more sensitive to HNO_3, and therefore NO_x. The results are shown in Appendix Figure S13. This contrasts the results for 2010 (shown in the Nenes reference, Figure 5(b)), where the majority of the data lie in a regime sensitive to both NH_3 and NO_x, though it is consistent with our understanding of the trends in aerosol sulfate and the relative abundances of NO_x and NH_3.

We stress that these results are more qualitative than quantitative, as the $PM_{2.5}$ speciated aerosol measurements are not known. However, the dynamics and, in particular, the trend over the last decade, are likely representative.

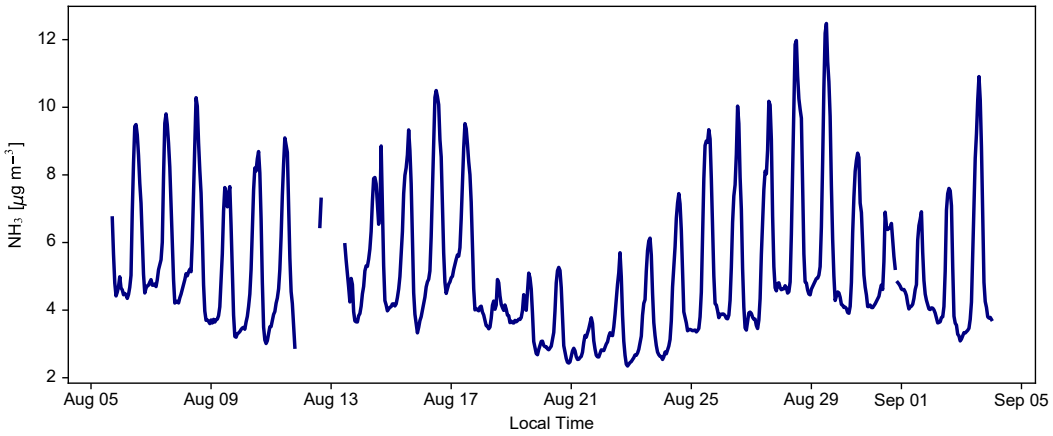

Appendix Figure S11: Time series of NH_3 measurements during the RECAP campaign (2021). Data were collected from a Picarro SI2103 Gas Concentration analyzer.

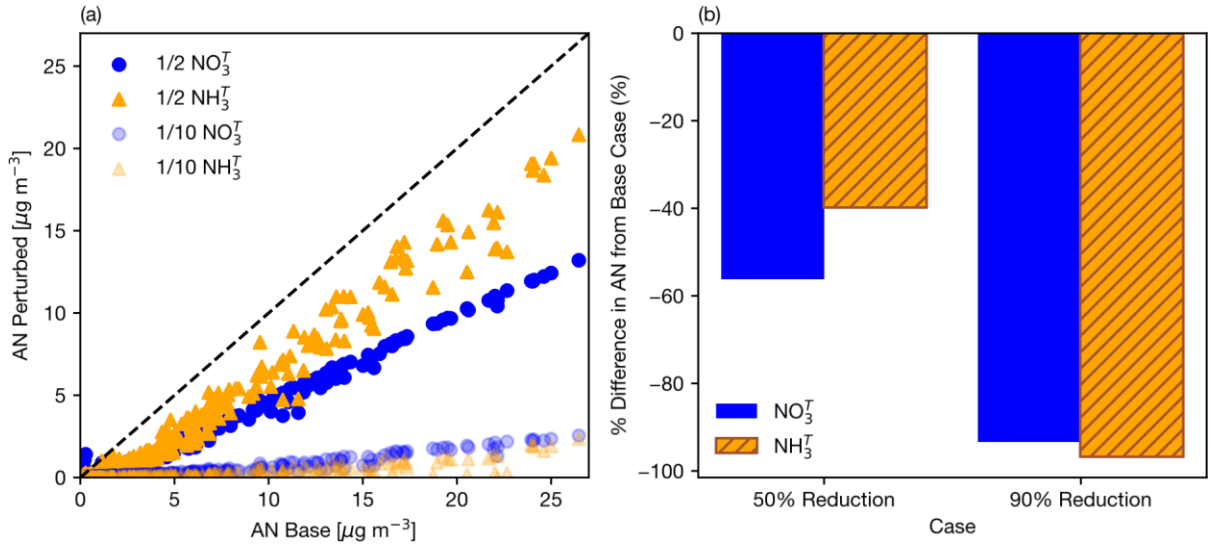

Appendix Figure S12: Nitrate sensitivity to precursor reductions. ISORROPPIA-II simulations are run for reduced total NO_3 and NH_3 concentrations, and the reduced total NO_3 and NH_4 cases are compared against the base case simulation. The campaign-wide results are show in (a) and the campaign average differences to the base simulation are shown in (b). Data are 1-hr time average.

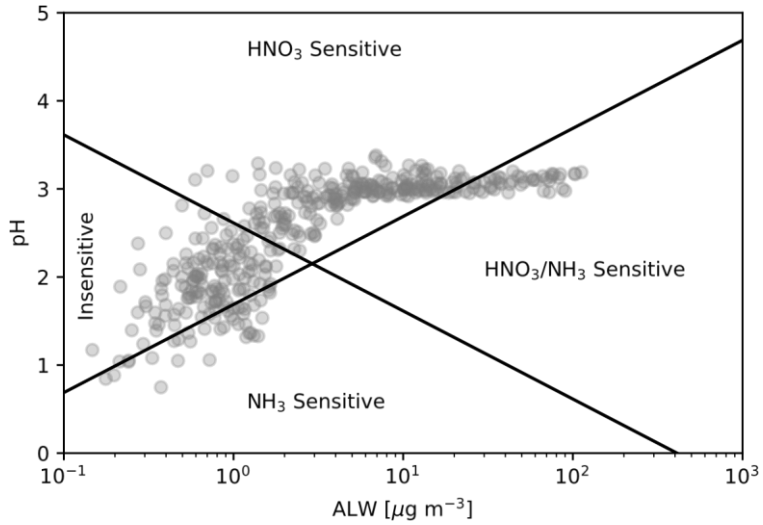

Appendix Figure S13: Sensitivity regime for nitrate aerosol Each data point is from the base case run of the RECAP campaign, and the sensitivity regime is identified after Nenes et al. 2020. The characteristic acidity curves are calculated from the campaign average aerosol liquid water predicted by ISORROPPIA-II. Data are 1-hr time average.

Health Impacts

As detailed in the Main Text, to understand how the use of uncorrected $PM_{2.5}$ concentrations impact estimated public health damages associated with $PM_{2.5}$ exposure, we calculate the population attributable fraction (PAF) with both uncorrected and corrected FRM PM measurements. Here, the PAF represents the proportion of total (all-cause) premature deaths in the population attributable to long-term exposure to $PM_{2.5}$ (Burnett et al. 2018). We consider annual average concentrations as surrogates for long-term exposure, and we impose a log-linear relationship on relative risk (RR) estimates, that is:

$$\beta = \ln RR$$

$$PAF = 1 - \exp\left(-\beta \times PM_{2.5}\right)$$

where RR = 1.03 (95% CI: 1.01–1.05) per 5 μg m^{-3} $PM_{2.5}$. This RR estimate derives from a recent systematic review and meta-analysis from the Health Effects Institute, which assessed health impacts associated with long-term exposure to traffic-related pollution. While other RR estimates exist, the traffic-specific nature of our RR estimate is particularly relevant in the urban context of Los Angeles, where traffic is an important contributor to total $PM_{2.5}$ mass and trends (Hasheminassab et al. 2014b). We discuss these calculations in the Main Text.

$PM_{2.5}$ mass, rather than number or composition, is currently the regulated quantity in the U.S. and many other parts of the world. However, while all components are associated with elevated mortality (Wyzga and Rohr 2015), growing evidence generally supports differential toxicities of individual $PM_{2.5}$ components. Generally, the strongest associations of $PM_{2.5}$ components and mortality are found for fossil fuel combustion (i.e., coal and traffic) components, with crustal and biomass components are generally less strongly associated with mortality (Thurston et al. 2016; Colonna et al. 2022; Wang et al. 2022). While understanding differential toxicities of components is still an emerging field, having observations and semi-empirical datasets based on observations that reflect the actual composition is a prerequisite for linking composition with adverse health effects.

CPF Analysis

In the absence of strong Santa Ana winds, which flush out the LA basin, we don't expect transport to play a dominant role in nighttime aerosol observations. This contrasts with the daytime, where in Pasadena, for instance, the urban plume arrives in the mid-afternoon due to southwesterly prevailing winds, driving up aerosol concentrations with secondary aerosol. To investigate the hypothesis that secondary nitrates are not primarily driven by longer-range (10s km) transport, we performed a conditional probability function (CPF) analysis on the Pasadena ACSM dataset. In brief, this is a receptor modeling approach which uses joint observations of concentration, wind speed, and wind direction to identify the local and long-range sources of air pollutants (Uria-Tellaetxe and Carslaw 2014). Concentration data are mapped to wind speed and direction using a Generalized Additive Model (GAM). A threshold for concentration is then set to identify dominant emissions sources at that interval (e.g., a source contributing to the 90th percentile of observed concentrations, like a stack plume from a coal-fired power plant vis-a`-vis SO_2 concentrations). These functions are viewed on a radial plot (similar to a wind rose) for visual interpretation.

We target the 90th percentile of nighttime ammonium nitrate concentrations (8.5 μg m^{-3}), which reveals that the footprint of ammonium nitrate production is generally local and independent of wind direction, shown in Appendix Figure S14. This footprint suggests that the production of ammonium nitrate is generally local, so calculating the relationship between the gas-phase pre- cursors and observed aerosol concentrations (as in Figure B2 in the Main Text) is not appreciably confounded by transport of either aerosol or gas-phase species.

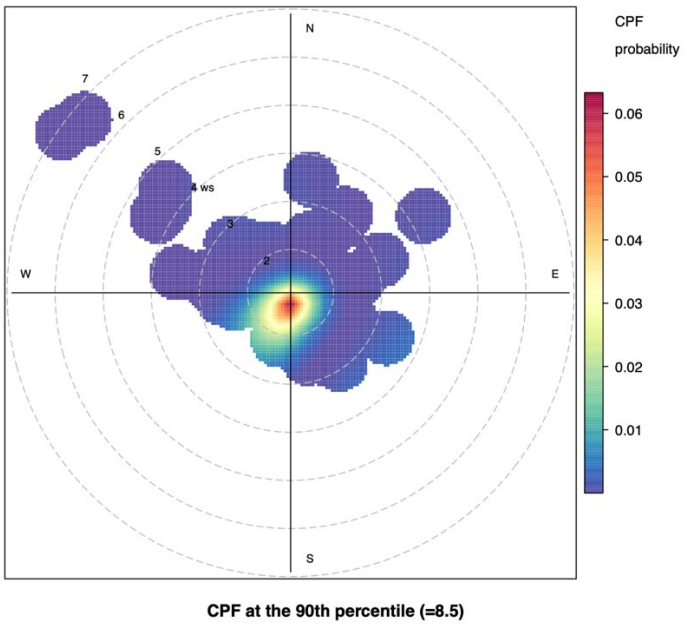

Appendix Figure S14: CPF plot of the 90th percentile ($\geq$ 8.5 μg m^{-3}) for nighttime ammonium nitrate during the Pasadena 2023 campaign. Wind speed is the radial axis, and the color corresponds to the CPF probability for ammonium nitrate.

CEPAM Inventory

The California Emissions Projection Analysis Model (CEPAM2019v1.03) was used to determine relative trends in NO_x and NH_3 emissions. Data were accessed for LA County in the summer, winter, and annual mean (it is expected equinox seasons will track the annual mean) for the years 2000 to 2023. The results are shown in Appendix Figure S12. We observe a robust decline in NO_x emissions over this time span (over 60%), but variable and roughly constant NH_3 emissions. Specifically for NH_3, it could possibly be argued that sub-selected to just the last decade, NH_3 emissions are increasing. While the model outputs in [ton day^{-1}], we have converted to [mol day^{-1}] for ease of comparison on a molecule-by-molecule basis. To do this for NOx, we have taken two limits to give us bounds on the emission: one where we assume all NO_x is emitted as NO and another where all NO_x is emitted as NO_2. It is apparent that NO_x emissions outnumber NH_3 emissions by roughly a factor of 10, though when considering atmospheric transformations, it is apparent that these two species may exist in relatively close abundances on a mole-for-mole basis, and so it is not immediately intuitive that the LA basin should be limited with respect to ammonium nitrate by either one of these precursors.

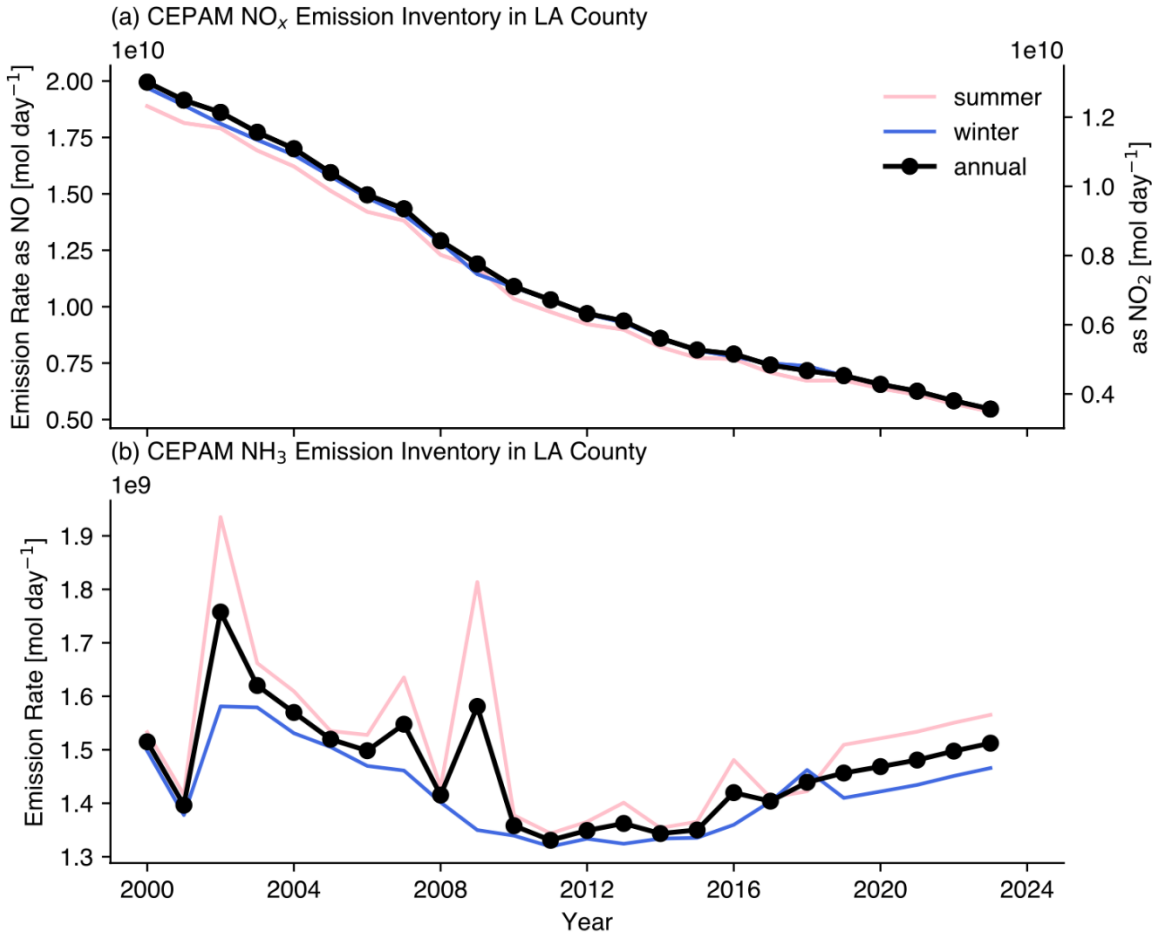

Appendix Figure S15: Time series of NO_x and NH_3 emissions in LA County, provided by the California Emissions Projection Analysis Model (CEPAM2019v1.03). Emissions are reported in [ton day^{-1}] and here converted to [mol day^{-1}]. For NO_x, we convert to the limit cases of either NO_x emitted all as NO or all as NO_2.

CMAQ EQUATES

EPA's Air QUAlity TimE Series Project (EQUATES) is a series of model runs by the EPA's CMAQ model, generated for the purpose of understanding trends in air quality Agency 2021. These data are available from their website and were accessed on July 1, 2024. We compared EQUATES output data for Pasadena with FRM data collected at that location, the results shown in Appendix Figure S16. Specifically, we sub-selected from spring and early summer (March — June), when we expect ammonium nitrate concentrations to be high, for the years 2014 — 2019.

In general, the model agrees well with the FRM data, and the observed ammonium nitrate mass fractions predicted by CMAQ are significantly lower than observed by the ACSM in 2023. Because it is likely the

FRM is evaporating ammonium nitrate, we expect that CMAQ is under-predicting the amount as well. Over this period, we calculated the expected and observed production of nitrate aerosol, similar to our calculations with the ACSM and AMS datasets. These results are shown in Appendix Figure S17.

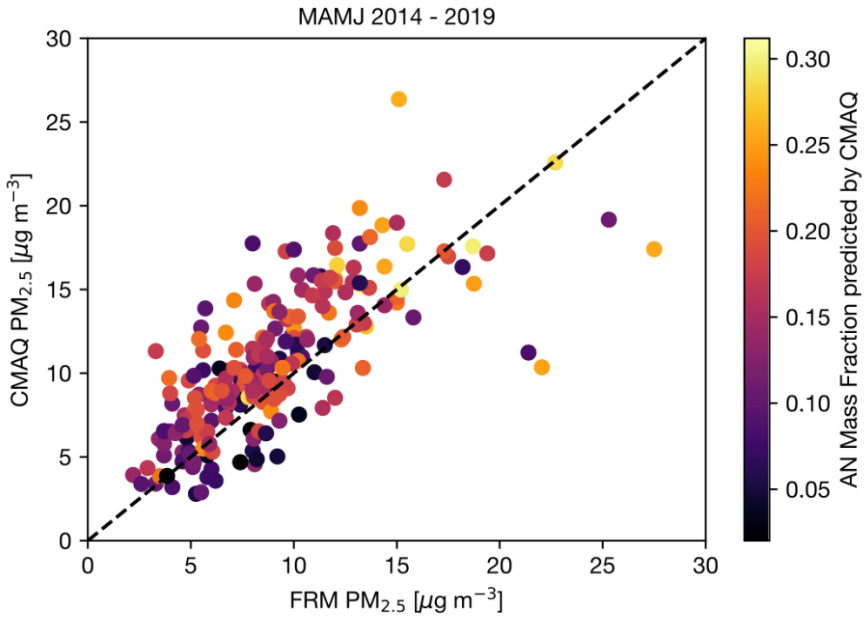

Appendix Figure S16: Scatter plot of time series measurements of FRM PM2.5 in Pasadena and CMAQ output for Pasadena from 2014 to 2019. Data are for the months of March, April, May, and June and colored by the predicted mass fraction of ammonium nitrate (AN) reported by CMAQ. Each data point represents a single 24 hr period (when an FRM measurement was made, which is not every day).

While RH can play some role in preventing nitrate aerosol, as expected, what is more obvious is that the model almost never converts the available nighttime gas-phase NO_3 reservoir into nitrate aerosol. This underestimated nitrate production has been documented in other chemical transport models, such as GEOS-CHEM (Heald et al. 2012).

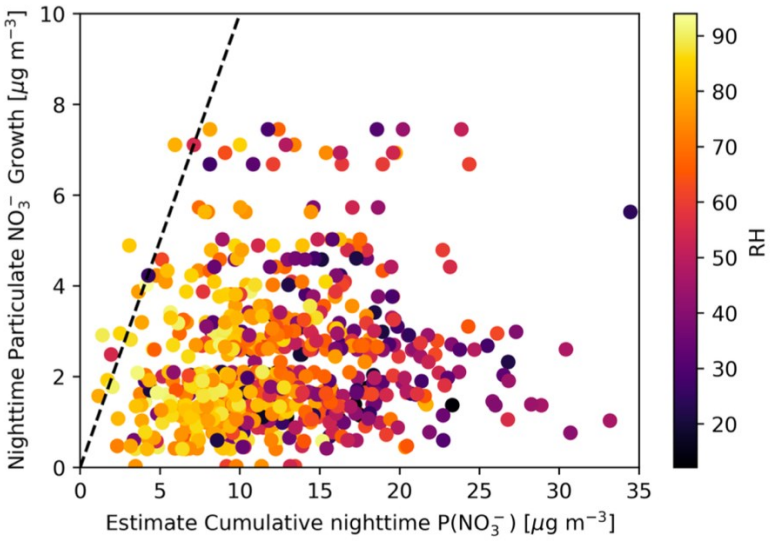

Appendix Figure S17: Scatter plot of estimated nighttime production of nitrate aerosol and produced nitrate aerosol predicted by CMAQ, colored by relative humidity.

AQMD Data

From EPA data we retrieve and resample PM and trace gas data from various sites in the South Coast Air Quality Management District (SCAQMD), and we correct these data for ammonium nitrate partitioning as described in the FRM section. Data were accessed through the Air Quality and Meteorological Information System (AQMIS). Figures are shown below:

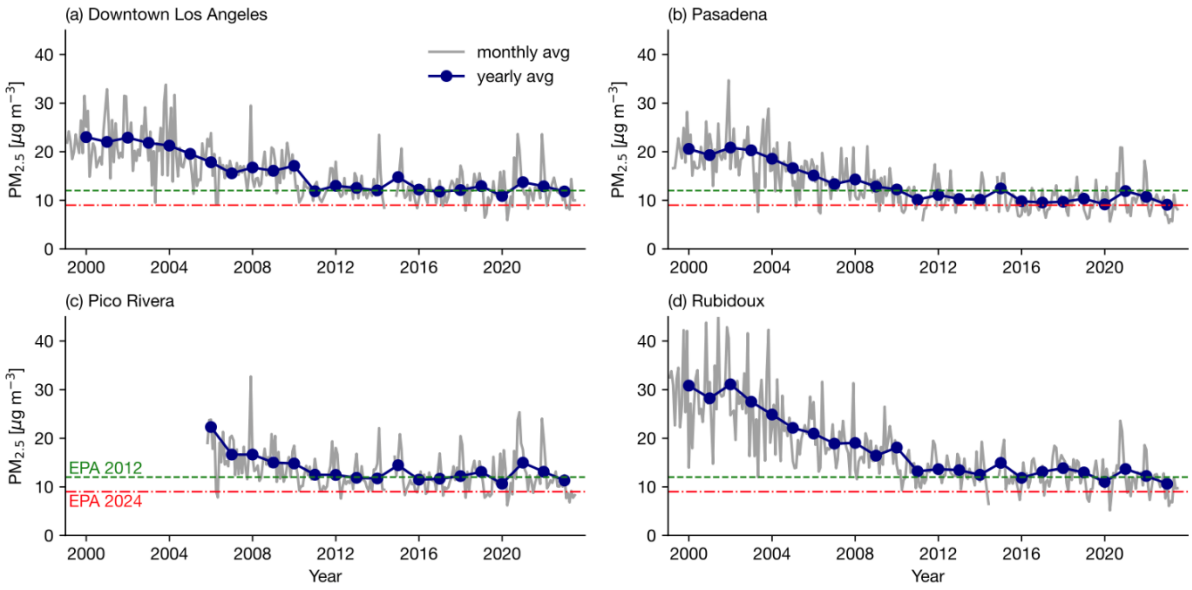

Appendix Figure S18: Time series of $PM_{2.5}$ measured at various SCAQMD locations, aggregated to monthly (grey) and yearly (navy) averages. The green dashed line represents the EPA's 2012 NAAQS for annual-average PM (12 $\mu g\ m^{-3}$) and the red dash-dot line represents the EPA's 2024 strengthening of that standard (9 $\mu g\ m^{-3}$).

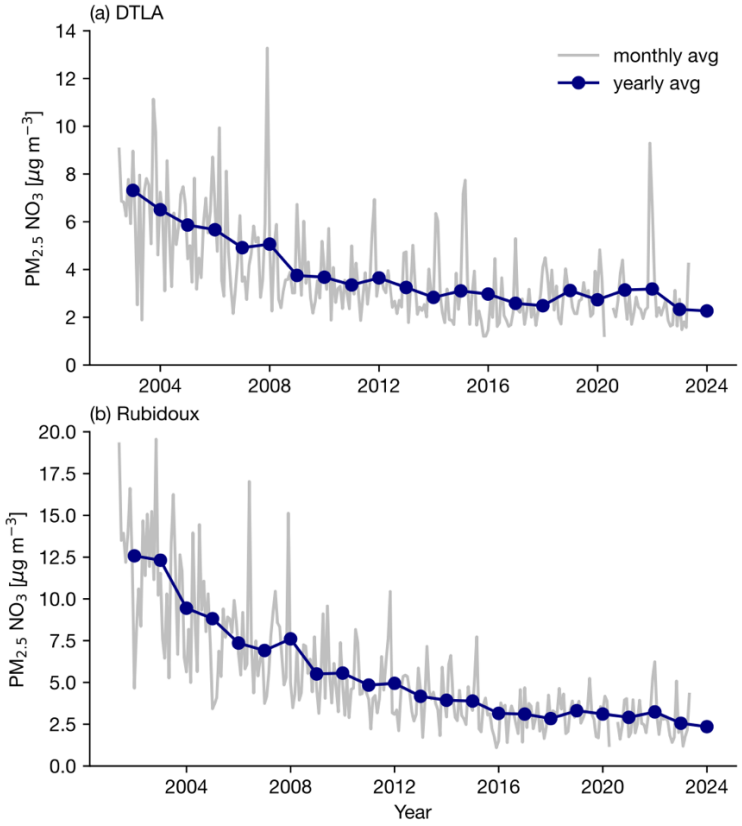

Appendix Figure S19: Time series of $PM_{2.5}$ NO_3 measured at various SCAQMD locations aggregated to monthly (grey) and yearly (navy) averages**.**

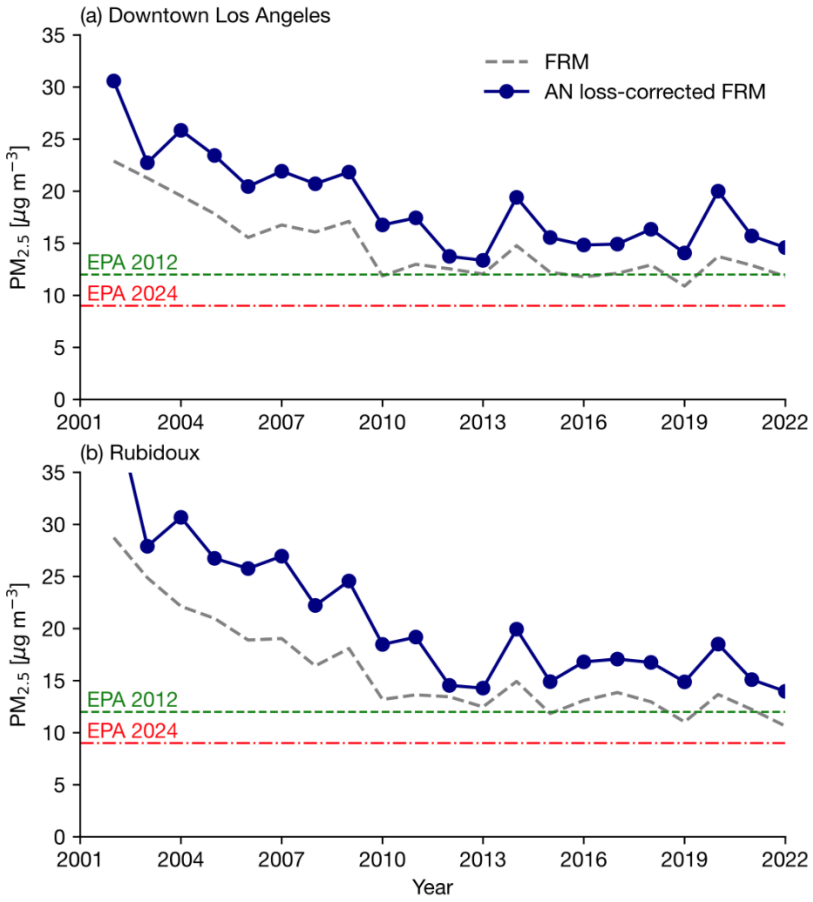

Appendix Figure S20: Time series of $PM_{2.5}$ measured at various SCAQMD locations, corrected for the loss of ammonium nitrate.

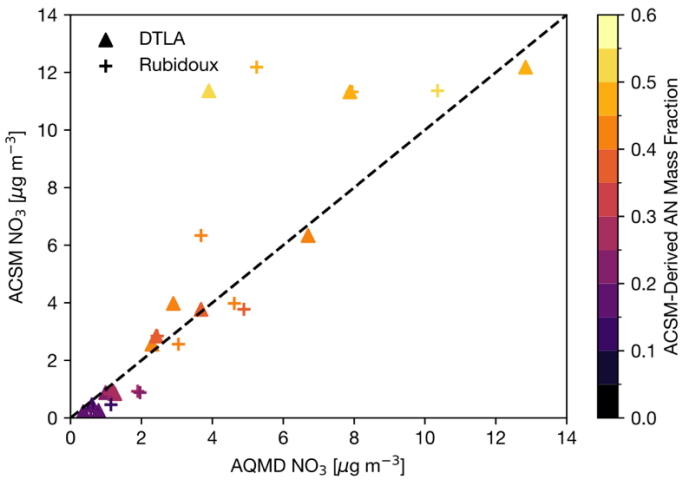

Appendix Figure S21: Comparison between ACSM particulate nitrate measurements in Spring of 2023 in Pasadena with filter measurements made by SCAQMD at two locations in Southern California, Riverside-Rubidoux (shown by the + marker) and Downtown LA (shown by the triangle marker). Points are colored by the ACSM-derived ammonium nitrate mass fraction. Each point is a 24-hr average.

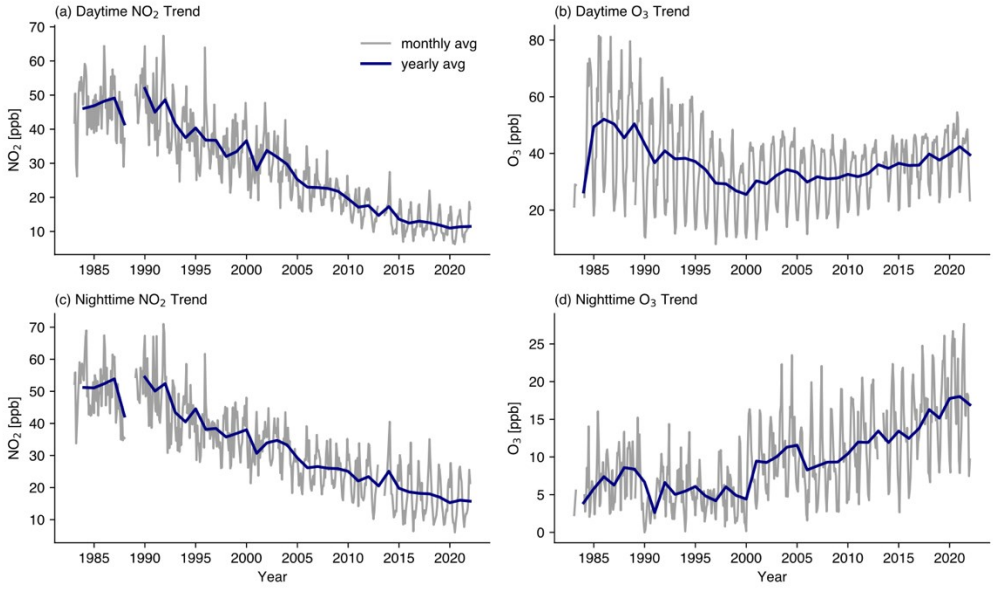

Appendix Figure S22: Time series of NO_2 and O_3 concentrations in Pasadena from AQMD, split to daytime and nighttime averaging.